

GFDL's CM2 Global Coupled Climate Models. Part III: Tropical Pacific Climate and ENSO

ANDREW T. WITTENBERG, ANTHONY ROSATI, NGAR-CHEUNG LAU, AND JEFFREY J. PLOSHAY

NOAA/Geophysical Fluid Dynamics Laboratory, Princeton University, Princeton, New Jersey

(Manuscript received 14 December 2004, in final form 14 May 2005)

ABSTRACT

Multicentury integrations from two global coupled ocean–atmosphere–land–ice models [Climate Model versions 2.0 (CM2.0) and 2.1 (CM2.1), developed at the Geophysical Fluid Dynamics Laboratory] are described in terms of their tropical Pacific climate and El Niño–Southern Oscillation (ENSO). The integrations are run without flux adjustments and provide generally realistic simulations of tropical Pacific climate. The observed annual-mean trade winds and precipitation, sea surface temperature, surface heat fluxes, surface currents, Equatorial Undercurrent, and subsurface thermal structure are well captured by the models. Some biases are evident, including a cold SST bias along the equator, a warm bias along the coast of South America, and a westward extension of the trade winds relative to observations. Along the equator, the models exhibit a robust, westward-propagating annual cycle of SST and zonal winds. During boreal spring, excessive rainfall south of the equator is linked to an unrealistic reversal of the simulated meridional winds in the east, and a stronger-than-observed semiannual signal is evident in the zonal winds and Equatorial Undercurrent.

Both CM2.0 and CM2.1 have a robust ENSO with multidecadal fluctuations in amplitude, an irregular period between 2 and 5 yr, and a distribution of SST anomalies that is skewed toward warm events as observed. The evolution of subsurface temperature and current anomalies is also quite realistic. However, the simulated SST anomalies are too strong, too weakly damped by surface heat fluxes, and not as clearly phase locked to the end of the calendar year as in observations. The simulated patterns of tropical Pacific SST, wind stress, and precipitation variability are displaced 20°–30° west of the observed patterns, as are the simulated ENSO teleconnections to wintertime 200-hPa heights over Canada and the northeastern Pacific Ocean. Despite this, the impacts of ENSO on summertime and wintertime precipitation outside the tropical Pacific appear to be well simulated. Impacts of the annual-mean biases on the simulated variability are discussed.

1. Introduction

The tropical Pacific is a key region for understanding and predicting global climate variations. With its intense precipitation and enormous size, this region directly and indirectly affects weather, ecosystems, agriculture, and human populations around the globe (Diaz and Markgraf 2000; Hsu and Moura 2001; Alexander et al. 2002; Barsugli and Sardeshmukh 2002). In particular the El Niño–Southern Oscillation (ENSO), which paleorecords suggest has existed for at least 10^5 yr (Cole 2001; Tudhope et al. 2001), is the earth's dominant cli-

mate fluctuation on interannual time scales [see special issue of the *Journal of Geophysical Research* (1998, Vol. 103, No. 7)]. Routine observations of the tropical Pacific (McPhaden et al. 1998), operational forecasts of ENSO and its global impacts (Latif et al. 1998; Goddard et al. 2001), and projections of future climate change (Easterling et al. 2000; Houghton et al. 2001) all underscore the importance of ENSO for climate monitoring, climate forecasting, and climate change. Thus a key test of a comprehensive global coupled general circulation model (CGCM) is whether it provides accurate simulations of tropical Pacific climate and ENSO.

Yet realistic CGCM simulations of the tropical Pacific have proved elusive. Strong ocean–atmosphere interactions in this region, which lend predictability to the atmosphere, also make the climate system highly sensitive to errors in the component models. Air–sea feedbacks can amplify small biases and generate sizable

Corresponding author address: Dr. Andrew T. Wittenberg, NOAA/Geophysical Fluid Dynamics Laboratory, Princeton University, P.O. Box 308, Forrestal Campus, U.S. Route 1, Princeton, NJ 08542.
E-mail: Andrew.Wittenberg@noaa.gov

drifts away from the observed mean state (Dijkstra and Neelin 1995; Philander et al. 1996). These drifts, in combination with approximations in the model physics, can then affect the simulation of ENSO (Moore 1995; Fedorov and Philander 2000; Wittenberg 2002), as well as the phenomena that perturb ENSO—such as the Madden-Julian oscillation and westerly wind bursts in the west Pacific. Climate drifts can also change how ENSO influences tropical precipitation, altering the atmospheric teleconnections that carry the ENSO signal around the globe.

As documented in recent intercomparison studies (AchutaRao et al. 2000; Latif et al. 2001; AchutaRao and Sperber 2002; Davey et al. 2000, 2002; Hannachi et al. 2003), common problems in CGCMs include 1) a cold sea surface temperature (SST) bias in the equatorial central Pacific; 2) a warm SST bias near the coast of South America; 3) an overly strong (“double”) inter-tropical convergence zone (ITCZ) south of the equator in the eastern Pacific; 4) a diffuse oceanic thermocline; 5) a weak Equatorial Undercurrent (EUC); 6) a weak annual cycle of SST and winds in the eastern Pacific, or a semiannual cycle instead of annual; 7) a westward shift of ENSO anomaly patterns relative to observations; 8) a weak ENSO with a period that is too short and too regular in time; 9) ENSO SST anomalies that are not skewed strongly enough toward warm events; and 10) a lack of adequate phase locking of ENSO to the annual cycle.

Development of the latest Geophysical Fluid Dynamics Laboratory (GFDL) CGCMs, Climate Model versions 2.0 (CM2.0) and 2.1 (CM2.1), represents a significant effort toward addressing these problems—subject to the constraints of a global approach that also demands accurate simulations outside the tropical Pacific. A rather unusual aspect of this development has been the dedication of the component modelers to formulating a realistic fully coupled system, capable of simulating climate on time scales ranging from weeks to centuries (Delworth et al. 2006; Stouffer et al. 2006). The result is a unified model framework with significant utility for seasonal-to-interannual forecasts as well as projections of future climate change. The purpose of this paper is to evaluate the tropical Pacific climate, ENSO, and ENSO teleconnections in multicentury control integrations of these two new models, subject to 1990 radiative conditions. Results are shown from both models, because of their relevance to the community [both models are being used for the 2007 Intergovernmental Panel on Climate Change (IPCC) Assessment, and for operational ENSO forecasts; hindcast evaluation metrics and real-time forecasts are available online at http://www.gfdl.noaa.gov/~rgg/si_workdir/

Forecasts.html], for comparison (important differences between the models lend insight into the climate of the tropical Pacific), and for continuity (the models represent a bridge between past and future climate modeling at GFDL). The ENSO forecast skill of the models and the tropical Pacific response to future radiative forcings will be covered in future papers.

2. Models and observational datasets

a. Model description

The model formulations are described in detail by Delworth et al. (2006), so we need only comment here on a few aspects of particular relevance to the tropical Pacific.

The ocean components of CM2.0 and CM2.1 are known as Ocean Model versions 3.0 (OM3.0) and 3.1 (OM3.1; Gnanadesikan et al. 2006; Griffies et al. 2005). Both are based on Modular Ocean Model version 4 (MOM4) code, with 50 vertical levels and a $1^\circ \times 1^\circ$ horizontal B-grid telescoping to $1/3^\circ$ meridional spacing near the equator. The vertical grid spacing is a constant 10 m over the top 220 m and gradually increases to a maximum of roughly 370 m in the deepest parts of the ocean. Partial bottom cells are used to better represent the topography of the ocean floor. Subgrid-scale parameterizations include K-profile parameterization (KPP) vertical mixing (Large et al. 1994), neutral physics (Gent and McWilliams 1990; Griffies et al. 1998; Griffies 1998), and a spatially dependent anisotropic viscosity (Large et al. 2001). OM3.1 has reduced values of horizontal viscosity outside the Tropics and has a constant neutral diffusivity of $600 \text{ m}^2 \text{ s}^{-1}$, which is generally larger than the nonconstant values used in OM3.0.

Air-sea fluxes are computed on the ocean model time step, which is 1 h in OM3.0 and 2 h in OM3.1. Insolation varies diurnally, and the shortwave penetration depth depends on a prescribed spatially varying climatological ocean color (Morel and Antoine 1994; Sweeney et al. 2005). Both ocean models have an explicit free surface, with true freshwater fluxes exchanged between the atmosphere and ocean. The surface wind stress is computed using the velocity of the surface wind relative to the surface currents.

The primary difference between the CGCMs is in the atmosphere component. CM2.0 uses the AM2p12b atmosphere model [GFDL Global Atmospheric Model Development Team (2004, hereafter GAMDT-04), with modifications listed in Delworth et al. (2006)], which consists of a B-grid dynamical core with 24 vertical levels, 2° latitude by 2.5° longitude grid spacing, a K-profile planetary boundary layer scheme (Lock et al. 2000), relaxed Arakawa-Schubert convection (Moorthi

TABLE 1. Observations and reanalysis datasets used in this paper.

Abbreviation	Name	References	Providers	Epochs used
CMAP.v2	Climate Prediction Center (CPC) Merged Analysis of Precipitation	Xie and Arkin (1996, 1997)	NCEP, CPC, IRI	1979–2003
ER.v2	NOAA Extended Reconstructed SST, version 2	Smith and Reynolds (2003)	NCDC, CDC, IRI	1880/1954–2003, 1980–99
ERA-40	ECMWF 40-Year Reanalysis	Simmons and Gibson (2000)	ECMWF	1979–2001, 1980–99
ERBE/NCEP	Earth Radiation Budget Expt/NCEP fluxes, dated Mar 2003	Trenberth et al. (2001)	K. Trenberth and D. Stepaniak	Mar 1985–Feb 1989
FSU2	The Florida State University/Center for Ocean–Atmospheric Prediction Studies In Situ Objective Research Quality Tropical Pacific Pseudostress Analysis, version 1.1	Bourassa et al. (2001) and Smith et al. (2004)	FSU/COAPS	1979–2001
GFDL/ARCs	GFDL/Applied Research Centers ocean data assimilation	Derber and Rosati (1989)	GFDL	1980–99
GPCP.v2	Global Precipitation Climatology Project, version 2	Adler et al. (2003)	GSFC, NCDC, UMD, JISAO	1979–2000, 1979–2003
HOAPS-II	Hamburg Ocean Atmosphere Parameters and Fluxes from Satellite Data, version 2	Grassl et al. (2000)	Max Planck Institute	1987–2002
J-OFURO	Japanese Ocean Fluxes Using Remote Sensing Observations	Kubota et al. (2002)	SMST/Tokai University	1990–2001
NCEP1	NCEP–NCAR reanalysis	Kistler et al. (2001)	CPC, IRI	1951–2000
NCEP2	NCEP–DOE AMIP-II reanalysis	Kanamitsu et al. (2002)	NCEP, CDC	1979–2001
NCEP ODA	NCEP Pacific Ocean Data Assimilation	Behringer et al. (1998)	NCEP/CMB, IRI	1980–99
OL.v2	NOAA Optimum Interpolation SST, version 2	Reynolds et al. (2002)	CPC, NCEP/CMB, IRI	1982–2004
OSCAR	Ocean Surface Current Analyses Real Time	Bonjean and Lagerloef (2002)	NOAA, ESR	Nov 1992–Oct 2004
QuikSCAT	SeaWinds/QuikSCAT level 3.0	IFREMER/CERSAT (2002)	IFREMER/CERSAT	Dec 1999–Nov 2004
SOC	Southampton Oceanography Centre fluxes	Josey et al. (1998)	SOC	1980–97
SOCa	Southampton Oceanography Centre adjusted fluxes, solution 3	Grist and Josey (2003)	SOC	1980–93
TAO ADCP	Tropical Atmosphere Ocean acoustic Doppler current profilers	McPhaden et al. (1998)	PMEL/TAO Office	May 1988–Nov 2003
TAO FD	Tropical Atmosphere Ocean fixed-depth mechanical current meters	McPhaden et al. (1998)	PMEL/TAO Office	Mar 1980–Aug 2001
UWM/COADS	University of Wisconsin—Madison revised Comprehensive Ocean Atmosphere Data Set	da Silva et al. (1994)	UWM, NODC, IRI	1979–93

and Suarez 1992), and a simple local parameterization of the vertical momentum transport by cumulus convection. CM2.1 uses the AM2p13 atmosphere model, which has essentially the same spatial resolution and physical packages as AM2p12b, but substitutes a finite-volume dynamical core (Lin 2004). Other differences between the atmospheric models include a retuning of the cloud scheme and changes in the land model (Delworth et al. 2006).

The two coupled control simulations are initialized at

year 1 as described in Delworth et al. (2006) and then integrated forward in time subject to 1990 values of trace gases, insolation, aerosols, and land cover. No flux adjustments are employed. In what follows, model statistics are computed using the first 300 yr of each run.

b. Observational datasets

Table 1 lists the observational datasets used in this study. The abbreviations listed in the first column de-

note these datasets through the remainder of the paper. Monthly means are used except where otherwise noted.

3. Annual-mean fields

a. SST and precipitation

Figure 1 shows the annual-mean SST over the tropical Pacific from the models and observations. Each model shows a well-developed equatorial cold tongue, and a warm pool in the west that extends eastward along 5°–12°N. The west Pacific warm pools simulated by the models do not extend as far north as observed. As in many CGCMs, the simulated equatorial cold tongue is too strong and extends too far west. Difference plots (Fig. 2) show that the equatorial cold SST bias approaches 1°–2°C in the central–eastern Pacific for both models, and the simulated equatorial westward SST gradient is stronger than observed in the western and central Pacific. Near South America there is a strong warm bias, approaching 7°C at the Peru coast. The SSTs are also too warm in the central Pacific near 10°N. Away from the equator, the SSTs are generally warmer in CM2.1 than CM2.0 (see also Delworth et al.

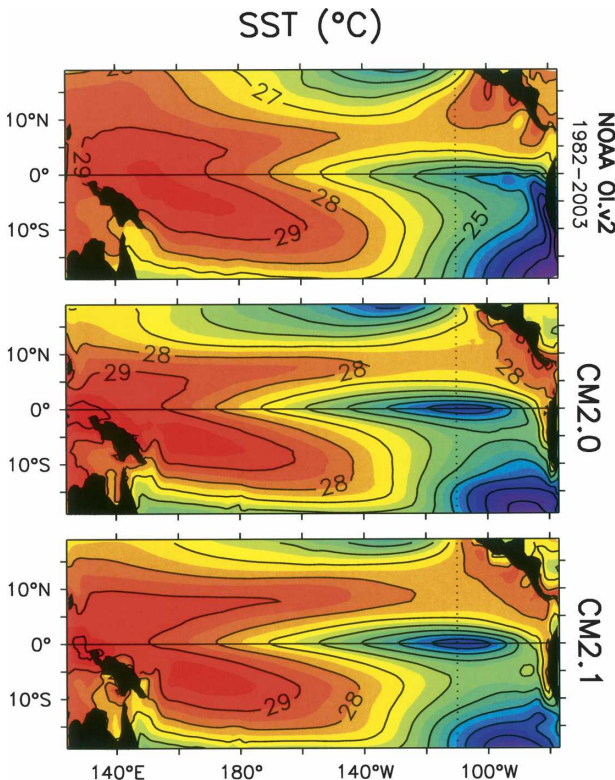


FIG. 1. Annual-mean SSTs (°C) over the tropical Pacific. Observations correspond to the 1982–2003 average from the OI.v2 analysis (see Table 1 for dataset abbreviations). Dotted line corresponds to the annual cycle section of Fig. 13.

SST differences (°C)

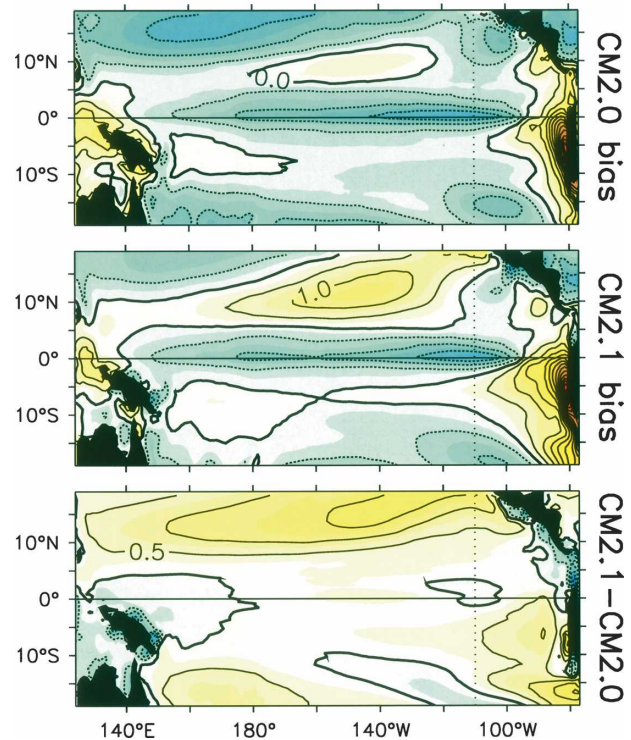


FIG. 2. (top), (middle) Annual-mean SST biases (°C) of the coupled simulations, with respect to the OI.v2 observations in the top panel of Fig. 1. (bottom) Difference between the CM2.1 and CM2.0 SSTs. Contour interval is 0.5°C, with shading incremented every half contour.

2006). There is little difference between the models in terms of their zonal SST gradient along the equator. However, CM2.1 does show a stronger northward SST gradient in the northern ITCZ region, and a weaker northward SST gradient in the eastern equatorial Pacific, than does CM2.0.

Figure 3 shows the annual-mean rainfall over the tropical Pacific. The models show strong precipitation in the far western Pacific and along the South Pacific convergence zone (SPCZ) and northern ITCZ regions. These features are generally stronger than observed, as is the “double ITCZ” in the east along 5°S. There is too much rainfall near New Guinea and South America, and too little rainfall along the equator in the central Pacific. The precipitation biases are largely coincident with local SST biases: there is too little precipitation on the equator where SSTs are too cold, and too much precipitation in the far west, far east, and off-equator where SSTs are too warm. Compared to CM2.0, CM2.1 shows less rainfall in the ITCZ, SPCZ, and western Pacific and more rainfall along the equator, all of which are in better agreement with the observations. How-

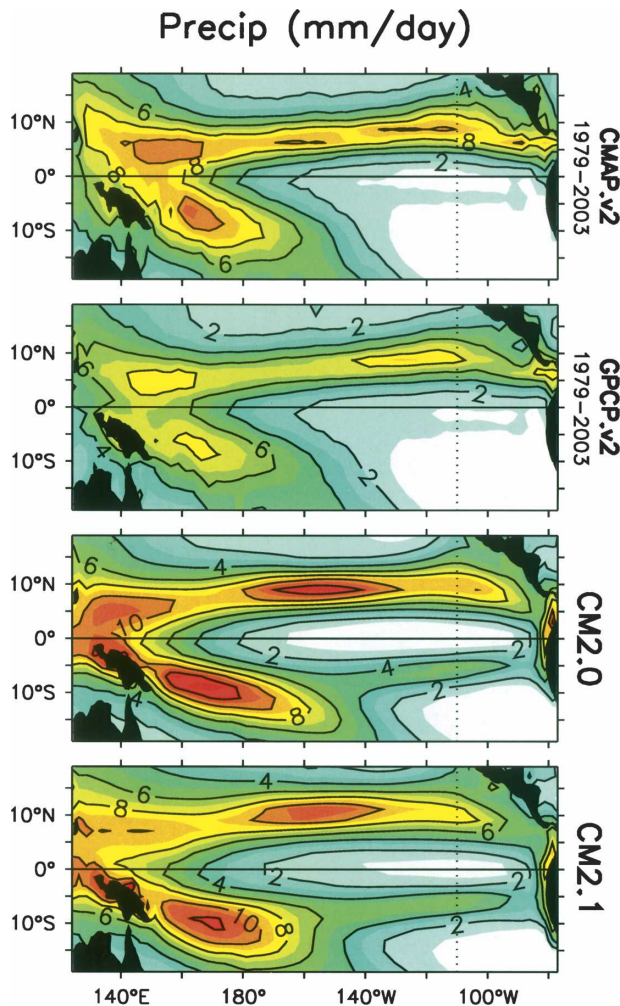


FIG. 3. Annual-mean precipitation (mm day^{-1}) over the tropical Pacific. Observations correspond to time averages from the CMAP.v2 and GPCP.v2 analyses.

ever, CM2.1 also shows a slightly stronger double ITCZ bias in the southeast, consistent with the weaker northward SST gradient in that region relative to CM2.0 (Fig. 2), and a slight northward shift of the northern ITCZ, consistent with the northward expansion of warm pool SST relative to CM2.0. Both of these latter features represent greater biases in CM2.1 than in CM2.0.

b. Surface wind stress

Figure 4 shows the zonal component of the annual-mean surface wind stress (τ_x). The mean equatorial τ_x is well simulated when compared with the 40-yr European Centre for Medium-Range Weather Forecasts (ECMWF) Reanalysis (ERA-40) observations, with peak easterlies of about 0.5–0.6 dPa occurring near 150°W and weak westerlies near the eastern and west-

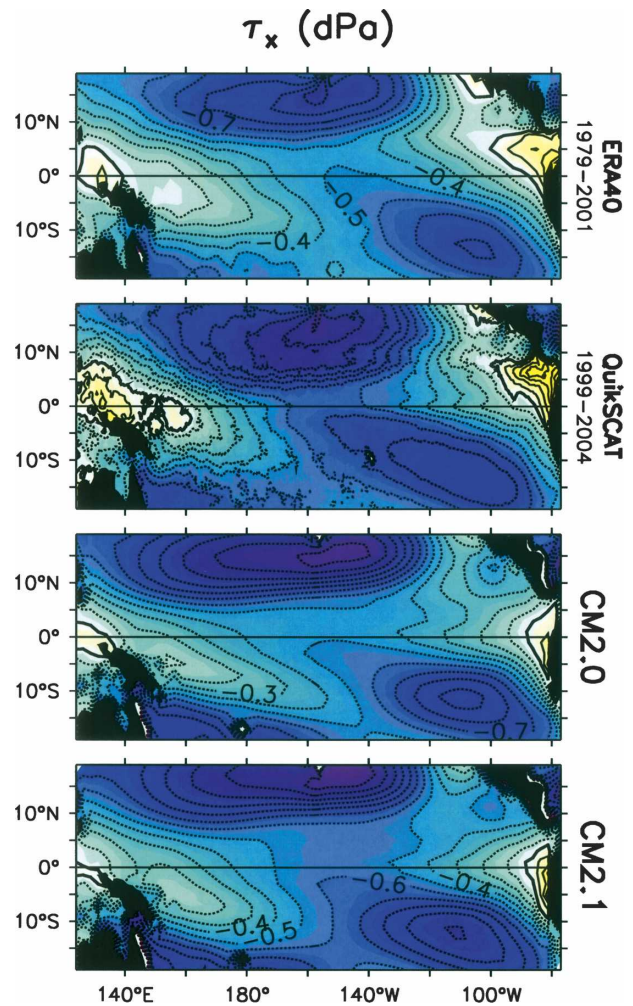


FIG. 4. Zonal component of the annual-mean surface wind stress (dPa). Observations correspond to ERA-40 stresses averaged over 1979–2001, and QuikSCAT stresses averaged Dec 1999 through Nov 2004.

ern boundaries. Note that the true mean wind stresses over the tropical Pacific are quite uncertain (Wittenberg 2004), with in situ and satellite observational products such as those from Florida State University (FSU; Stricherz et al. 1997; Bourassa et al. 2001) and the Special Sensor Microwave Imager (SSM/I; Atlas et al. 1996) giving somewhat stronger zonal stresses than ERA-40 over the 1979–2001 period. The recent Quick Scatterometer (QuikSCAT) observations (Fig. 4, second panel) also show stronger wind stresses throughout the central tropical Pacific, compared to ERA-40.

Figure 5 shows that CM2.1 generally has stronger central Pacific easterlies than CM2.0, except along 10°N due to the poleward shift of the northern core of the easterlies in CM2.1 relative to CM2.0. The differences in equatorial τ_x between CM2.0 and CM2.1 are not

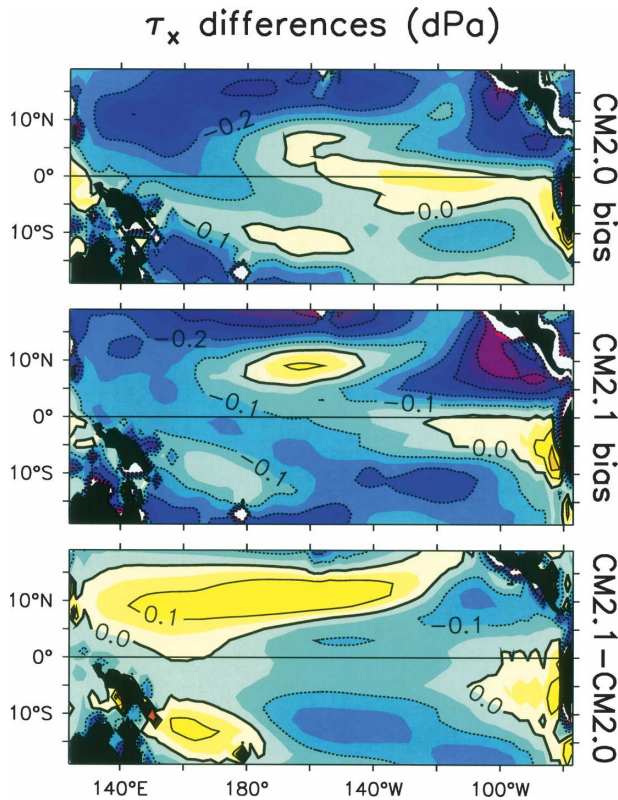


FIG. 5. (top), (middle) Annual-mean zonal wind stress biases (dPa) of the coupled simulations, with respect to the ERA-40 analysis shown in the top panel of Fig. 4. (bottom) Zonal wind stress difference between CM2.1 and CM2.0.

clearly linked to changes in the zonal SST gradient along the equator (Fig. 2), which suggests that this difference between the coupled models is due to the different formulations for the atmospheric components. In both models the equatorial easterlies are zonally broader than in the observations, with the western flank of the trades extending too far west. The off-equatorial easterlies also extend too far west and are too strong, giving rise to similar biases in the off-equatorial cyclonic wind stress curl. In the eastern Pacific along 0° – 5° N, the models reverse the meridional shear of τ_x compared to observations. Note that the τ_x differences between CM2.0 and CM2.1 are generally larger in the extratropics than in the Tropics (Delworth et al. 2006).

c. Surface heat fluxes

The annual-mean equatorial surface heat fluxes from the models and observations are shown in Fig. 6. The simulated fluxes are in reasonable agreement with the broad range of observational estimates. But in the central and eastern Pacific, there is 10 – 30 W m^{-2} too much

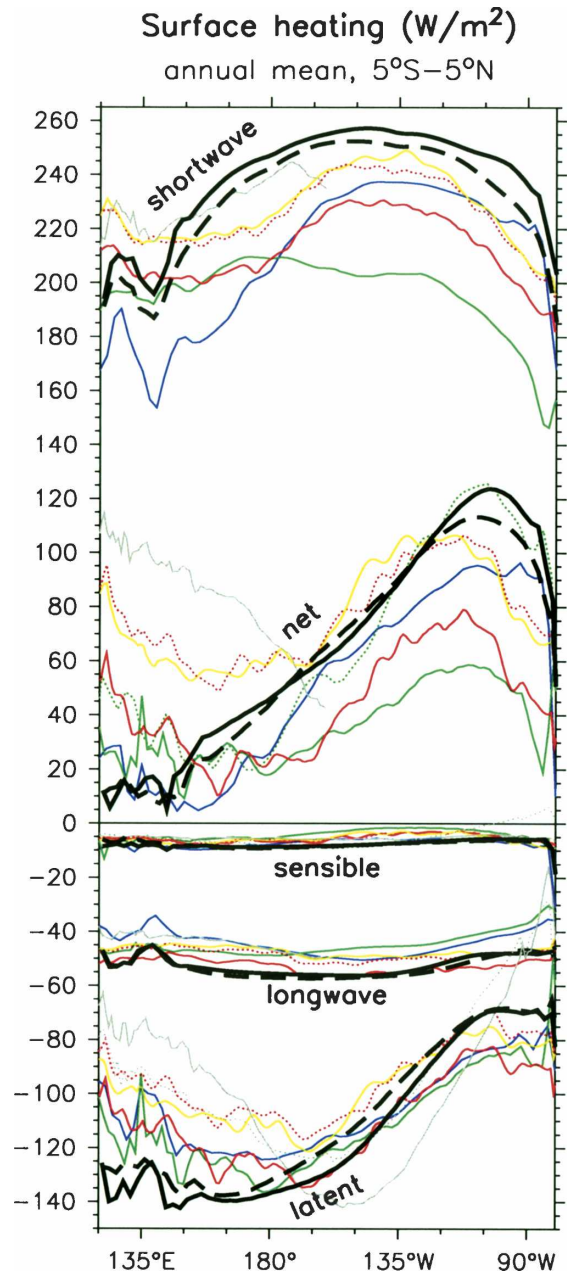


FIG. 6. Annual-mean surface heat fluxes over the Pacific, averaged over 5°S – 5°N . Thick lines are the simulations from CM2.0 (dashed) and CM2.1 (solid). Thin lines are observational estimates from ERA-40 (1979–2001) in blue; NCEP2 reanalysis (1979–2001) in solid green; the ERBE/NCEP net surface flux (Mar 1985–Feb 1989) in dotted green; SOCa climatology (1980–97) in solid red; UWM/COADS (1979–93) in yellow; J-OFURO (all available years during 1990–2001) in solid gray; and HOAPS-II (1987–2002) in dotted gray.

solar heating and 5 – 10 W m^{-2} too much longwave cooling in the models. Along with the slight underestimate of precipitation at the equator (Fig. 3), both the cloud fraction and cloud optical thickness are underestimated

in the central–eastern equatorial Pacific—particularly for low stratus near the eastern boundary (not shown). The total atmospheric column liquid water in the central–eastern equatorial Pacific is only $15\text{--}30\text{ g m}^{-2}$ for the coupled models, versus $40\text{--}70\text{ g m}^{-2}$ for satellite estimates (Greenwald et al. 1993; Weng et al. 1997). The coupled models also exhibit a cold bias through much of the tropical troposphere, which along with the deficit of low clouds could explain the overly strong longwave cooling of the surface. We note that these biases are also present in stand-alone integrations of the individual atmospheric models (GAMDT-04).

In the western–central Pacific, where the simulated trade winds are too strong (Fig. 5), there is $10\text{--}30\text{ W m}^{-2}$ more evaporative cooling in the models than observed. Conversely, in the east Pacific where the southeasterly trades are too weak (Fig. 13c), there is less evaporative cooling than in most of the observational estimates.

Both coupled models underestimate the fractional coverage by low-lying marine stratus clouds near the Pacific coasts of North and South America (not shown). In satellite and surface observations (Warren et al. 1988; Norris 1998; Rossow and Schiffer 1999; Hahn et al. 2001), the long-term, annual-mean low cloud coverage near these coasts generally exceeds 20%–30% north of the equator and 40%–50% south of the equator; the coupled models produce 5%–15% and 10%–30%, respectively. This underestimate of low cloudiness near the eastern boundary regions is also apparent in stand-alone AGCM integrations (GAMDT-04). Subsequent coupled feedbacks (Ma et al. 1996; Philander et al. 1996) can then exacerbate the coastal warm SST bias (Fig. 1) and further reduce the cloudiness, wind speed, evaporation, and upwelling near the model coasts.

The net heating in Fig. 6 is the sum of the shortwave, longwave, latent, and sensible components. In the west Pacific there appears to be too little net heating in the models, despite the SST cold bias—suggesting that the excessive evaporation may be partly to blame for the cold bias in the west. Likewise, weak evaporation and excessive insolation contribute to the overly warm SSTs near the South American coast. In the central equatorial Pacific the strong insolation *mitigates* the overly intense cold tongue in the models, implying that the cold bias in the central equatorial Pacific must be driven by ocean dynamical cooling rather than errors in the air–sea heat fluxes.

At the equator CM2.1 shows increased insolation—despite slightly more precipitation—than does CM2.0. CM2.1 also shows stronger evaporation (due to stronger easterlies) over the central Pacific. Although the

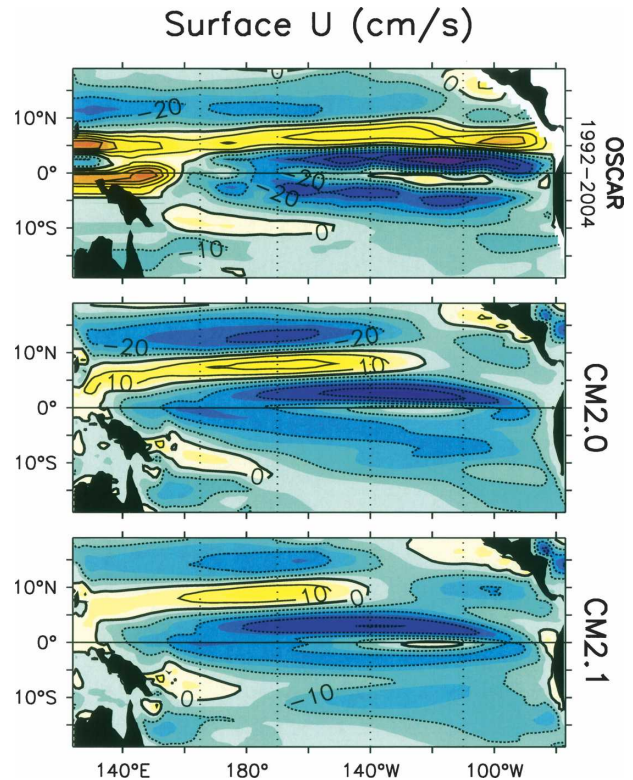


FIG. 7. Annual-mean surface zonal currents (cm s^{-1}) for the tropical Pacific. Observations correspond to the OSCAR analysis, averaged Nov 1992 through Oct 2004. Dotted lines correspond to the equatorial TAO mooring longitudes in Fig. 8.

solar and evaporative heat flux differences between the models nearly cancel over the central basin, the increased shortwave in CM2.1 does produce more net heating in the western and eastern equatorial Pacific, where CM2.1 is cooler than CM2.0. The net heat flux difference thus acts mainly to oppose the SST differences between the models.

Apart from the cloudiness biases along the equator and eastern boundary, the errors in tropical Pacific annual-mean precipitation, surface wind stress, and surface heat fluxes are much reduced when the atmospheric models are forced with observed SSTs (GAMDT-04; Delworth et al. 2006). Thus a majority of the coupled model biases appear to arise from climate drift, associated with the strong air–sea feedbacks over the tropical Pacific.

d. Ocean currents

The annual-mean surface zonal currents from the models and observations are shown in Fig. 7. In the western central Pacific the models capture the general structure of the observed surface currents, including the

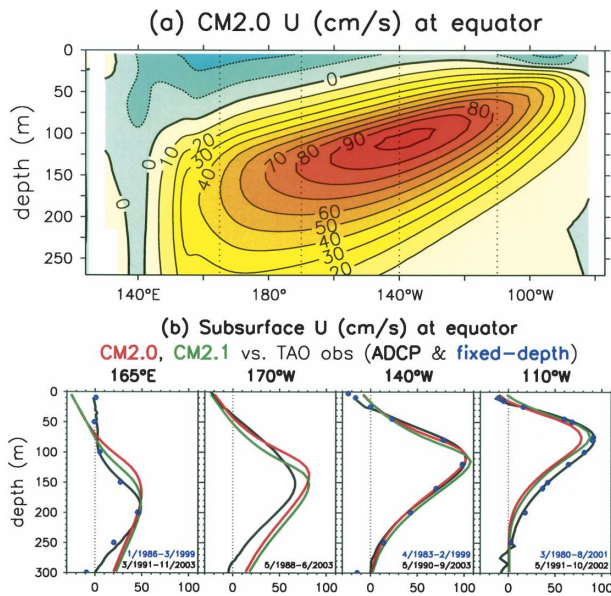


FIG. 8. Annual-mean zonal currents (cm s^{-1}) at the equator: (a) mean values for CM2.0; (b) mean values at the four longitudes marked in (a), from CM2.0 (red), CM2.1 (green), TAO ADCP (black), and TAO FD (blue dots).

westward South Equatorial Current (SEC), which straddles the equator; the westward North Equatorial Current (NEC) between 10° – 20° N; and the eastward North Equatorial Countercurrent (NECC), which sits between the SEC and NEC. The simulated currents, however, are displaced 20° – 30° west of the observed currents, and in the eastern Pacific the NECC does not extend to the Central American coast as in the observations. The simulated SEC is meridionally too wide; for example, in CM2.1 along 110° W, there are westward currents of magnitude $>10 \text{ m s}^{-1}$ extending between 16° S and 12° N, instead of between 10° S and 5° N as observed. On the other hand, the off-equatorial peaks of the SEC in the east Pacific, along 5° S and 3° N, are weaker than observed. In general the annual-mean surface currents are weaker in CM2.1 than in CM2.0, despite the stronger annual-mean τ_x in CM2.1.

In both models, the meridional shear of the zonal surface currents ($\partial_y u$) is much weaker than observed in the eastern tropical Pacific—which may partly explain the much weaker tropical instability wave (TIW) amplitudes in CM2.0 and CM2.1 compared to observations (not shown). The weak $\partial_y u$, in turn, is probably due to insufficient annual-mean wind stress curl in the east (Figs. 4 and 5).

Figure 8 shows the subsurface structure of the mean zonal currents at the equator. Compared to observations, both models show a good simulation of the an-

nual mean Equatorial Undercurrent, especially at 140° W where the observed and simulated currents reach a peak value of slightly over 1 m s^{-1} . At 110° W the simulated EUC is slightly too weak, while farther west it is too strong and vertically too broad. At 165° E there is excessive vertical shear of the zonal currents over the top 100 m, associated with the SEC that extends too far west in the models (Fig. 7). CM2.1 and CM2.0 produce very similar simulations of the EUC, with CM2.1 slightly deeper in the west and stronger in the east because of the stronger annual-mean τ_x in that model (Figs. 4 and 5).

e. Subsurface temperatures

Figure 9 shows the simulated Pacific upper-ocean temperatures along the equator, compared to the GFDL/Applied Research Centers (ARCs) ocean analysis (data available online at <http://nomads.gfdl.noaa.gov>).¹ A surface cold bias is evident in the central Pacific, along with a warm bias below the thermocline in the east and west. The zonal-mean depth of the 20°C isotherm is nearly correct, but the zonal slope of the thermocline is slightly too strong, consistent with the overly broad zonal extent of the simulated equatorial easterlies. The thermocline is also slightly too diffuse in the vertical. Because of the overly strong equatorial upwelling, westward cold advection, and evaporation driven by the strong simulated easterlies, the warm pool in the west does not extend far enough out into the basin. Near South America there is strong stratification in the models compared to the ocean analysis, with a surface warm bias sitting directly above a cold bias at 30 m. Through and below the main thermocline, CM2.1 is cooler in the eastern/central Pacific and warmer in the west than CM2.0.

Figure 10 shows the upper-ocean temperatures averaged zonally across the Pacific basin. Above 75 m, both models exhibit a zonal-mean cold bias except in the vicinity of the ITCZ (8° – 10° N) and near the surface south of the equator. Between 75 and 250 m, the models show a cold bias in the south and a warm bias in the north, associated with a meridional flattening of the isotherms compared to the ocean analysis. Especially in CM2.1, the simulated thermocline is more symmetric about the equator than observed. The strongest biases lie near the ITCZ, where the isotherms in the models

¹ Observed SSTs and temperature profiles assimilated into MOM4, using the three-dimensional variational scheme of Derber and Rosati (1989).

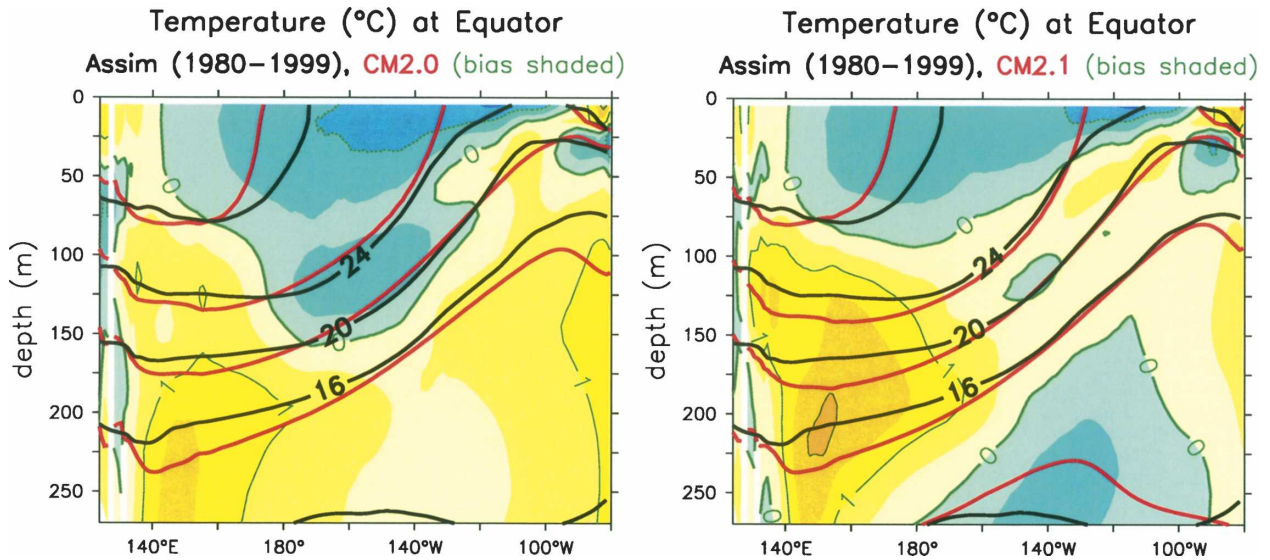


FIG. 9. Annual-mean Pacific Ocean temperatures ($^{\circ}\text{C}$) along the equator. Black contours indicate “observed” values from the GFDL/ARCs ocean analysis, red contours the coupled model solution, and green contours–shading the mean temperature bias of the model relative to GFDL/ARCs.

do not bow upward as strongly as in the analysis, consistent with the weak NECC in the models (Fig. 7). The zonal-mean warm bias at this location approaches 4°C in CM2.1, compared with 2°C for CM2.0. The next largest biases lie near the models’ southern double ITCZ between 5° and 10°S (Fig. 3). Below 200 m, CM2.1 shows mostly cooler zonal-mean temperatures than CM2.0.

The simulated ocean subsurface temperatures show somewhat larger differences when compared with the

National Centers for Environmental Prediction (NCEP) Pacific Ocean Data Assimilation (ODA) of Behringer et al. (1998), which has a tighter annual-mean thermocline at the equator. The analog of Fig. 9 shows increased cold/warm biases above/below the thermocline, a larger difference in the zonal thermocline slope, and stronger stratification biases above 50 m near the South American coast. Away from the equator, however, the coupled model differences with the NCEP ODA look very similar to Fig. 10.

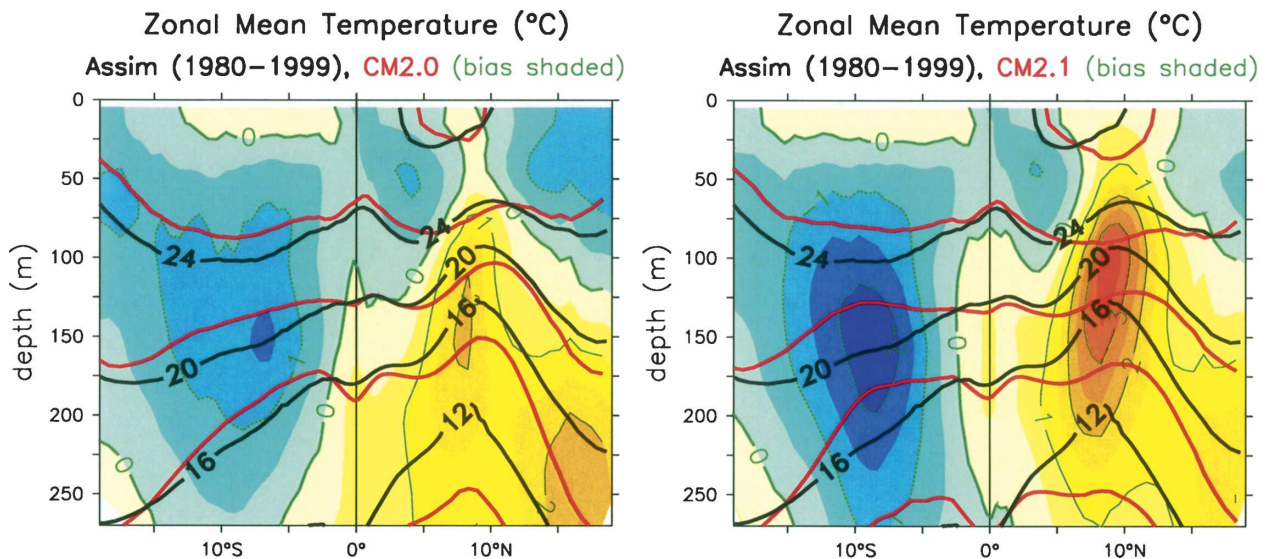


FIG. 10. Same as in Fig. 9, except for ocean temperatures averaged zonally across the Pacific basin.

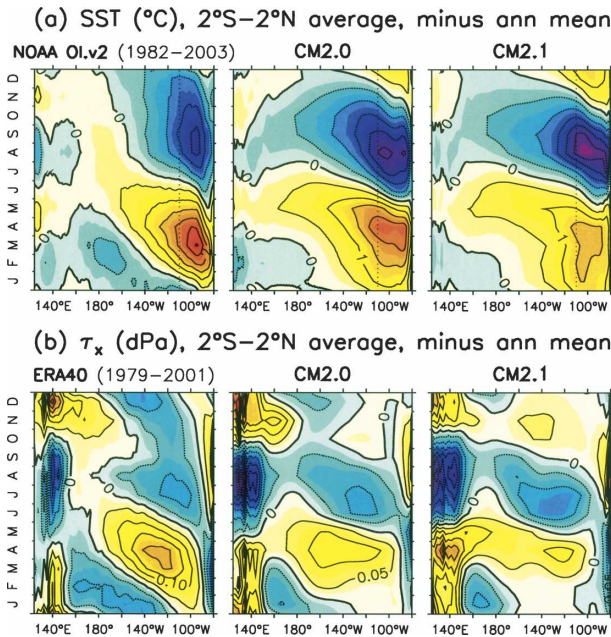


FIG. 11. Annual cycle, averaged over 2°S–2°N, of (a) SST (°C) and (b) zonal wind stress (dPa). Annual-mean values are subtracted. Observations correspond to OI.v2 for SST and ERA-40 for wind stress.

4. Seasonal cycle

a. Equator

The annual cycle of equatorial Pacific SST is shown in Fig. 11a. In qualitative agreement with observations, both models show a robust westward-propagating annual cycle of SST in the eastern and central Pacific, and a semiannual cycle in the west. The zonal-mean annual cycle of SST is somewhat too strong in the models (see also Fig. 19), since between April and November the annual cycle of SST propagates too far west—with 0.5°C anomalies extending west of the date line instead of staying east of 160°W as observed. On the other hand, the observed 0.5°C cold anomalies near the date line in March are not seen in the models, and in general the cold phase of the annual cycle terminates about 2 months too early. In the east the warm season peak is too weak compared to the cold season peak, especially in CM2.1. Apart from the warm peak in boreal spring, the phase of the seasonal cycle in the east is also shifted 1–2 months earlier in the models than in observations.

Such problems simulating the equatorial annual cycle are common among CGCMs (Latif et al. 2001; Meehl et al. 2001) and highlight the difficulty in simulating the complex interaction of poorly resolved and poorly observed processes in the eastern Pacific—such as the air–sea fluxes of heat and momentum, the oceanic upwelling and mixing into the surface mixed layer, and the

meridional heat transport by TIWs (Kessler et al. 1998; Wang and Fu 2001). In CM2.0 and CM2.1, for example, the TIWs (not shown) are weaker than observed—implying reduced equatorial heating during the cold phase of the annual cycle, and likely contributing to the excessive annual cooling of equatorial SST in the simulations.

Figure 11b shows the annual cycle of τ_x near the equator. The models capture some of the observed relaxation of the trade winds during boreal spring, though it is underestimated and exhibits less of the westward propagation seen in the observations. In the east Pacific, the strengthening of the trades during boreal summer is reasonably well captured, although the models show a westward shift of the seasonal cycle relative to the observations. CM2.1 shows stronger peak easterly deviations than observed in boreal summer. The models display more of a semiannual cycle than observed, with weaker-than-observed trades in boreal autumn and winter. In contrast, the simulated annual cycle of τ_x in the far western Pacific is stronger than observed.

The seasonal cycle of τ_x is tightly linked with that of the Equatorial Undercurrent (Fig. 12). Although the

U (cm/s) deviations at 0°N, 140°W

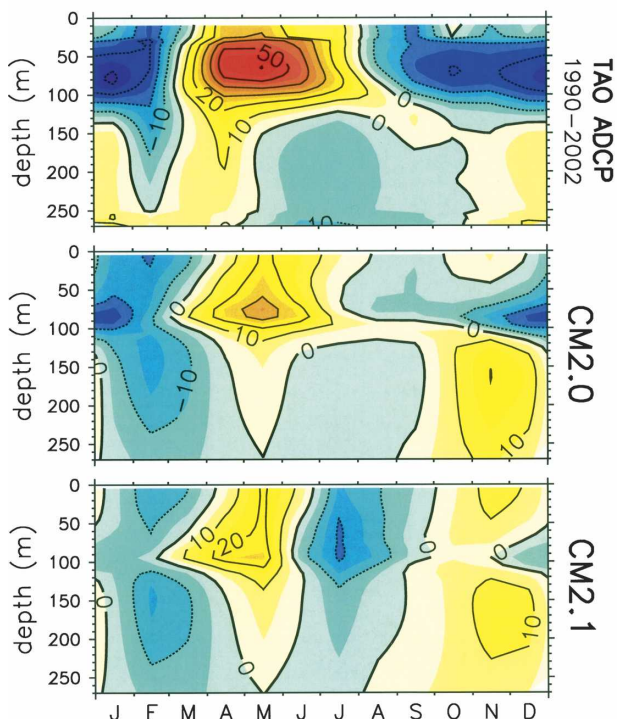


FIG. 12. Annual cycle of zonal currents (cm s^{-1}) on the equator at 140°W. Annual mean is subtracted. Observations correspond to the 1990–2002 climatology from the TAO ADCP moored at 140°W.

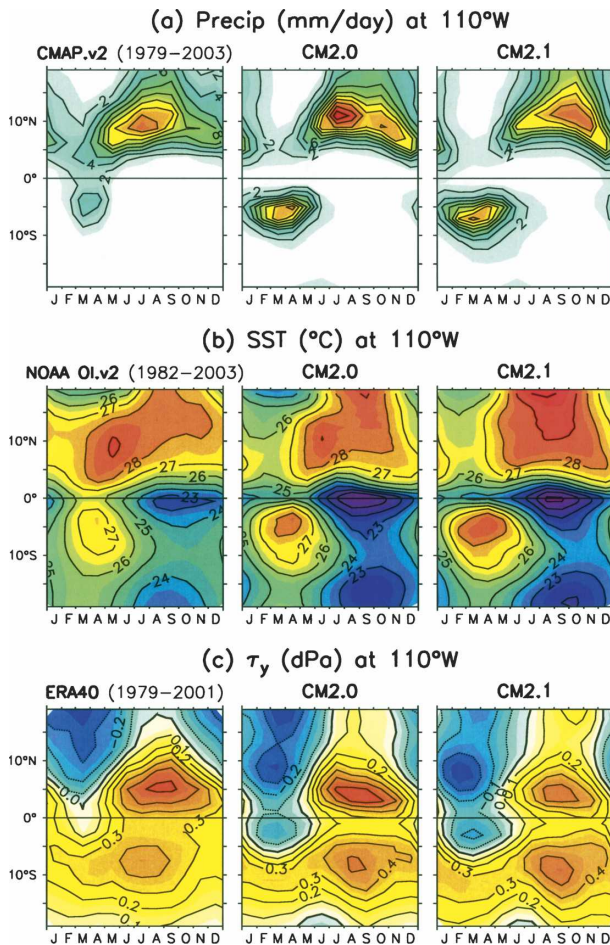


FIG. 13. Annual cycle along 110°W of (a) rainfall (mm day^{-1}), (b) SST ($^{\circ}\text{C}$), and (c) meridional wind stress (dPa).

models do well with the annual-mean strength of the EUC (Fig. 8), they underestimate the strength of its annual cycle. That the May peak of the EUC is too weak, especially in CM2.1, is likely tied to the lack of a sudden weakening of the equatorial trade winds early in the year (Fig. 11b). Above 100 m both models show more of a semiannual cycle than observed, consistent with the excessive semiannual signal in the simulated winds.

b. East Pacific

The annual cycle of precipitation in the eastern tropical Pacific is shown in Fig. 13a. The observations show a maximum north–south asymmetry of SST and rainfall during boreal summer and autumn, when the ITCZ is strongest. In March–April, the precipitation is weaker and more symmetric about the equator, with substantial precipitation observed even at the equator. While CM2.0 and CM2.1 capture most of these features, there are some obvious problems. In the Southern Hemi-

sphere, both CM2.0 and CM2.1 rain too much and too far south in boreal spring, at the expense of spring precipitation at the equator and in the northern ITCZ. CM2.0 captures the observed July peak in ITCZ rainfall but overestimates its magnitude, while CM2.1 has roughly the right magnitude but shows the peak occurring 3 months too late.

Many of the errors in the simulated annual cycle of precipitation in the east Pacific are coupled to errors in the annual cycle of SST (Fig. 13b). The observed SSTs show a strengthening of the cold tongue in boreal autumn, and a weakening in boreal spring; in March the observed climatological SSTs approach 26.5°C at the equator, but the warmest SSTs remain north of the equator. In the models the climatological equatorial SSTs stay below 25°C all year, and in March the warmest SSTs are south of the equator. The models also show too much of a cold tongue/ITCZ SST contrast in boreal autumn, when the ITCZ region is 1°C too warm and the cold tongue is 2°C too cold.

The seasonal biases in SST and precipitation are likewise tied to the atmospheric meridional circulation in the eastern Pacific (Fig. 13c). At the equator, the observed climatological τ_y weakens significantly in boreal spring but remains southerly all year. In contrast, the models exhibit a reversal of the equatorial τ_y in boreal spring, in tandem with the reversal of the simulated meridional gradient of SST. The minimum in τ_y at 2°S is more pronounced in the models than in observations, as is the local maximum of τ_y at 10°S , producing an overly strong wind convergence along 4° – 8°S that is linked to excessive precipitation during boreal spring (Fig. 13a). Compared to CM2.0, CM2.1 shows a slightly stronger March reversal of the meridional winds, and a stronger convergence of τ_y along 4° – 8°S .

5. ENSO

a. Spatial patterns

The spatial patterns of tropical Pacific interannual SST variability are shown in Fig. 14. In the observations, the interannual SST anomalies (SSTAs) are strongest in the eastern equatorial Pacific and along the coast of South America. The models shift this variability westward, and both models (especially CM2.1) overestimate the interannual variability of SST throughout most of the tropical Pacific.

To assess the simulated patterns of air–sea fluxes during ENSO, we invoke the Niño-3 index (SSTA averaged over the boxed area in Fig. 14: 5°S – 5°N , 150° – 90°W) as a proxy for the interannual evolution of

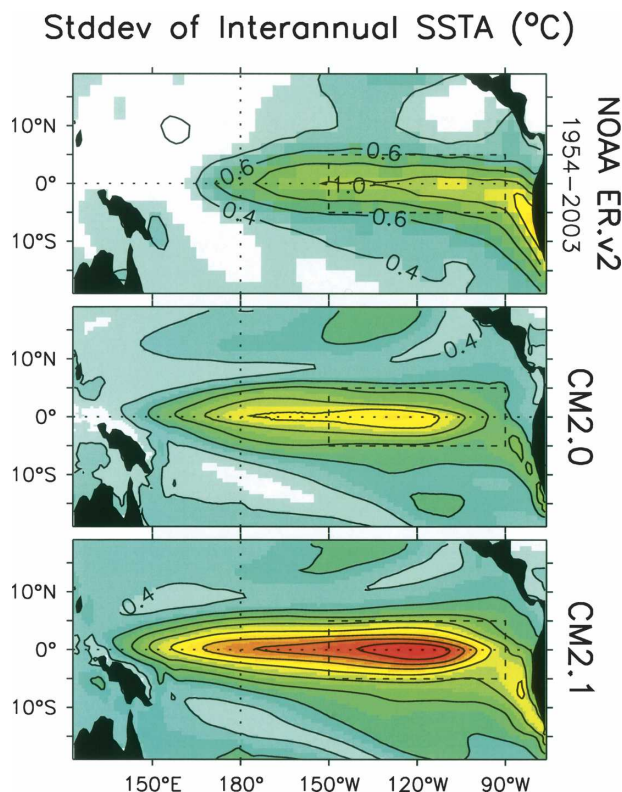


FIG. 14. Std dev of interannual SSTA anomalies ($^{\circ}\text{C}$). The anomalies are filtered via two applications of a 4-month running mean, transmitting 25% and 75% of the spectral amplitude at periods of 6.6 and 14 months, respectively. Observations correspond to the ER.v2 reconstruction. The dashed box in each panel indicates the Niño-3 region (5°S – 5°N , 150° – 90°W).

SSTA. Related indices, such as the Niño-3.4 average and the first principal component of tropical Pacific SSTAs correlate with Niño-3 at levels exceeding 0.95 for monthly values in the CM2 models and Extended Reconstructed SST version 2 (ER.v2) observations. One may therefore regress onto any of these indices and obtain very similar spatial patterns. We select Niño-3 because in the observations it has a high correlation with the first principal component of tropical Pacific SSTAs (0.98 correlation for monthly ER.v2 SSTAs, 1954–2003), making it a key target for coupled simulations. Niño-3 also sits in the overlap region of the observed and simulated SST variability, where the shallow thermocline exerts a strong influence on SST. Finally, the Niño-3 index is simple to compute, and permits straightforward comparisons with existing results in the literature.

Figure 15 shows the tropical Pacific precipitation regressed onto Niño-3 SSTAs. The observations indicate wet conditions along the equator in the central and

ENSO precipitation anomalies

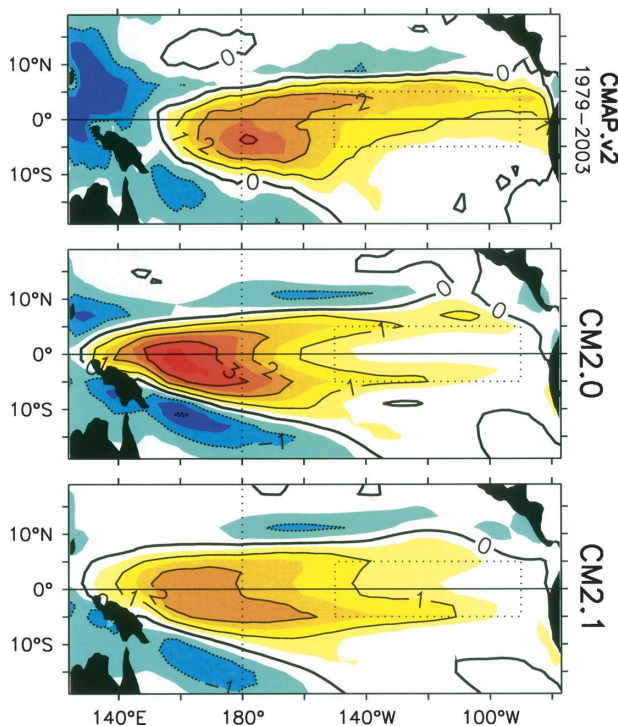


FIG. 15. Precipitation anomalies regressed onto Niño-3-averaged SSTA anomalies, all months included ($\text{mm day}^{-1} \text{ } ^{\circ}\text{C}^{-1}$). Observations correspond to the CMAP.v2 precipitation anomalies regressed onto the ER.v2 SSTAs for 1979–2003.

eastern Pacific during warm events, with peak rainfall anomalies just east of the date line. Meanwhile, drier-than-normal conditions prevail away from the equator and west of 155°E . In the eastern Pacific, the observed rainfall response is meridionally asymmetric, with wet conditions north of the equator but much less of a change in the south.

While the models do show increased rainfall over the central equatorial Pacific during warm events, there are clear differences with the observations. The precipitation response is too far west—consistent with the equatorial cold bias and the westward displacement of the annual-mean convection in the models (Figs. 1–3). In the east Pacific, the rainfall anomalies are too symmetric about the equator, probably due to the south-equatorial climatological warm bias and double ITCZ. There are also clear differences between the models themselves: in the west the peak rainfall response is stronger in CM2.0 than in CM2.1, while in the central/eastern Pacific the equatorial rainfall response is stronger in CM2.1.

The zonal wind stress anomaly (τ_x') response to

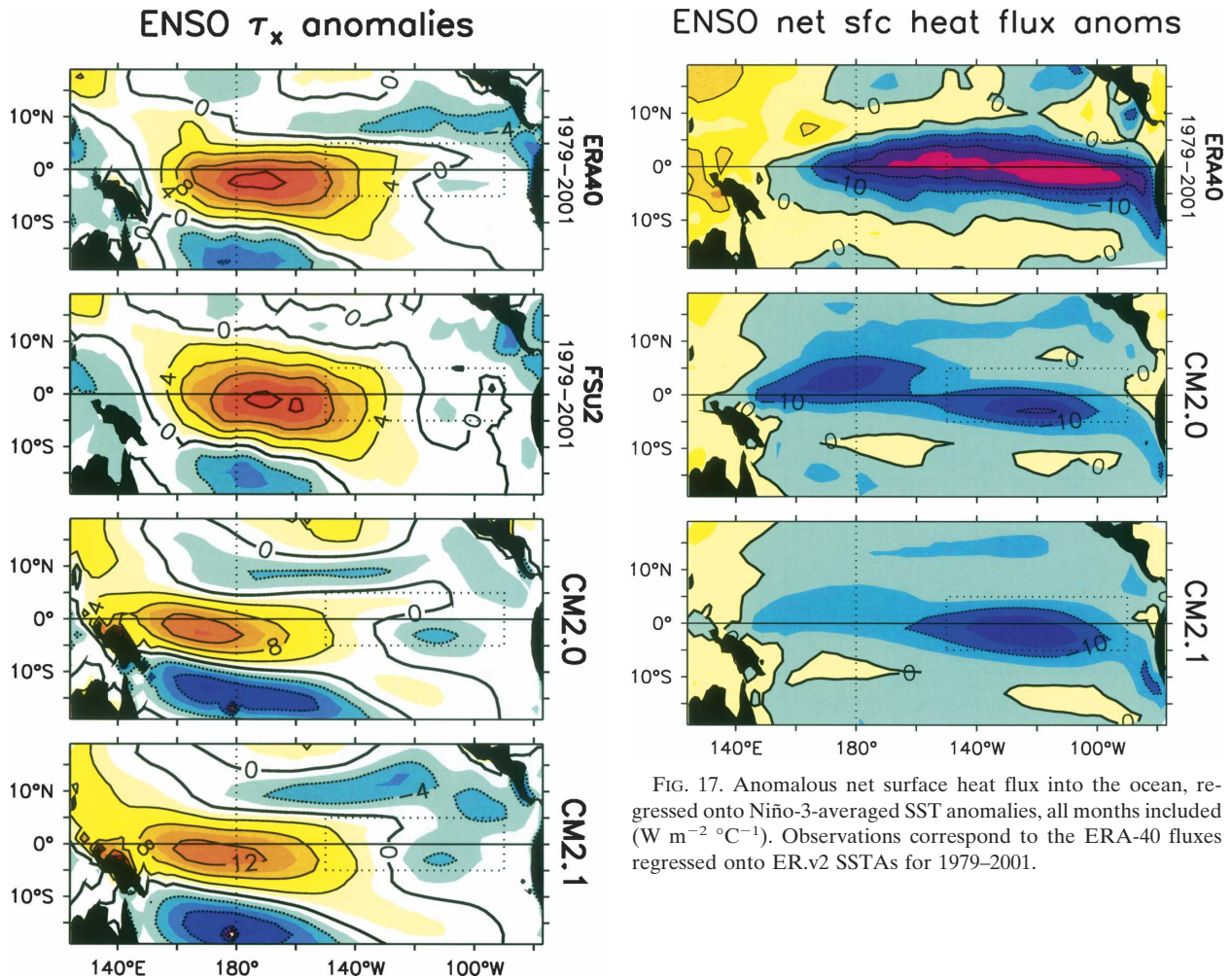


FIG. 16. Zonal wind stress anomalies regressed onto Niño-3-averaged SST anomalies, all months included ($\text{mPa } ^\circ\text{C}^{-1}$). Observations are regressed onto the ERA.v2 SSTAs for 1979–2001, and correspond to stress anomalies from ERA-40 and FSU2. Here the FSU2 “stress” consists of the FSU2 pseudostress multiplied by a constant air density $\rho_a = 1.2 \text{ kg m}^{-3}$ and drag coefficient $c_d = 1.3 \times 10^{-3}$.

Niño-3 SSTAs is shown in Fig. 16. The observations show westerly anomalies in the equatorial central Pacific during warm events, with the peak anomalies slightly east of the date line. The simulated equatorial westerly response is too weak and too far west, and in both models the easterly response south of the equator and in the east Pacific are too strong. The peak westerly τ'_x response along the equator extends farther east in CM2.1 than in CM2.0, consistent with the simulated climatological and anomalous precipitation differences between the two models (Figs. 3 and 15).

Figures 17 and 18 show the net surface heat fluxes regressed onto Niño-3 SSTAs. As noted by Barnett et al. (1991) and others, during a warm event the observed

FIG. 17. Anomalous net surface heat flux into the ocean, regressed onto Niño-3-averaged SST anomalies, all months included ($\text{W m}^{-2} \text{ } ^\circ\text{C}^{-1}$). Observations correspond to the ERA-40 fluxes regressed onto ERA.v2 SSTAs for 1979–2001.

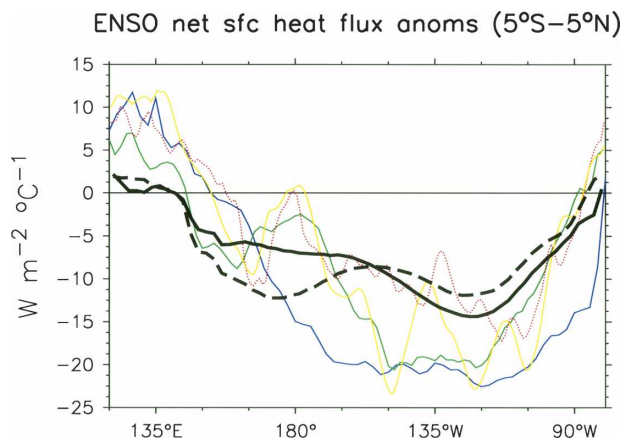


FIG. 18. Anomalous net surface heat flux into the ocean, averaged over 5°S–5°N, regressed onto Niño-3-averaged SST anomalies. All months are included in the regression ($\text{W m}^{-2} \text{ } ^\circ\text{C}^{-1}$). Thick lines are the model solutions from CM2.0 (dashed) and CM2.1 (solid). Thin lines are observational estimates (regressed onto ERA.v2 SSTAs) from the ERA-40 (1979–2001) in blue, NCEP2 (1979–2001) in green, SOC fluxes (1980–97) in dotted red, and UWM/COADS (1979–93) in yellow.

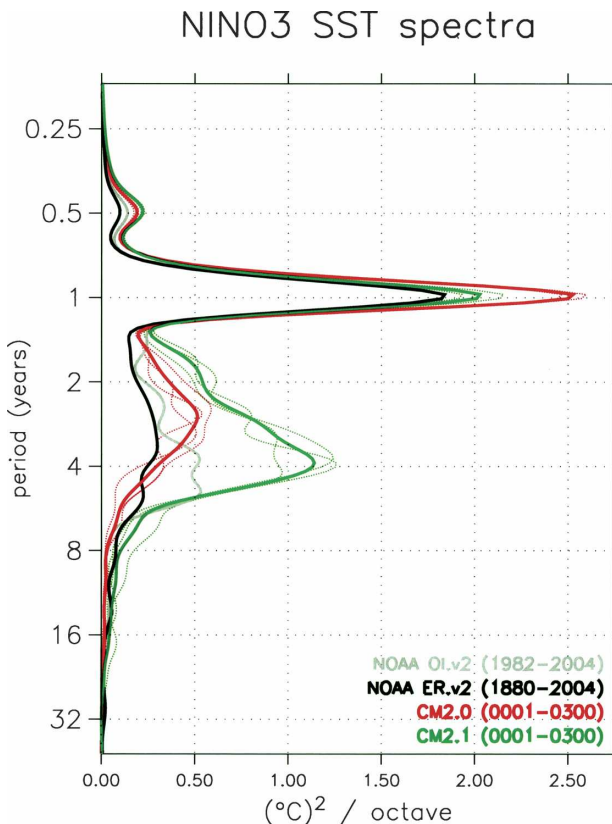


FIG. 19. Time-mean wavelet spectra ($^{\circ}\text{C}^2 \text{ octave}^{-1}$) for unfiltered Niño-3-averaged SSTs. Observations correspond to OI.v2 (1982–2004) in gray and ER.v2 (1880–2004) in black. Red and green lines correspond to the CM2.0 and CM2.1 spectra of Figs. 20c and 21c; thick lines are the simulated 300-yr mean spectra and thin dotted lines are spectra for the three individual centuries.

heat fluxes act to damp the zonal SSTA gradient (and thus τ_x anomalies), as a result of increased cloudiness and evaporation in the east Pacific and reduced cloudiness in the west. This damping effect is underestimated by the models, largely because the simulated convective response is too far west (Fig. 15). During warm events, the models show increased cloud shading in the far western Pacific instead of in the central Pacific as observed; and in the far eastern equatorial Pacific, the models actually have slightly increased insolation during warm events, instead of reduced insolation as observed. Neither model has sufficient heat flux damping of the cold anomalies off-equator and in the far western Pacific—where the SSTs are presumably most directly influenced by the surface heat fluxes due to the absence of strong equatorial upwelling, and where the atmosphere is presumably most sensitive to SSTAs due to the presence of warm mean SSTs and convergent surface winds. Note that CM2.1 has a somewhat weaker zonally integrated surface heat flux damping than does CM2.0.

b. Spectra

Figure 19 shows Niño-3 SST spectra for the models and observations. The observations display spectral peaks at annual and semiannual periods, as well as a broad peak in the interannual band between 2 and 5 yr. Although the models capture these features qualitatively, there are clear differences. The amplitude of the annual cycle is nearly correct in CM2.1, despite the bias toward the cold season evident in Fig. 11a. However, the annual cycle is too strong in CM2.0, and both models show stronger semiannual variability than in observations. Both models (especially CM2.1) have overactive ENSOs compared to long-term (1880–2004) observations but agree a bit more favorably with the amplitude observed over the last two decades.² The peak ENSO period in CM2.1 (3.9 yr) is a good match to the recent observations, while that in CM2.0 (2.7 yr) is too short.

The time evolutions of the simulated Niño-3 SST spectra are shown in Figs. 20 and 21. Both models exhibit strong interdecadal variations in the amplitude and period of ENSO, and interannual variations in the amplitude of the annual cycle. Rather than sustained oscillations, many of the simulated ENSO events appear to be episodic, spanning a range of frequencies over the course of one or two events. Both this episodic character and the interdecadal modulation of the dominant ENSO period contribute to the broad interannual peak in the time-mean spectrum.

It is clear from these figures that long time series are required to adequately characterize the ENSO spectrum in the models. In Figs. 20c and 21c, three time-averaged spectra are plotted—one for each third of the time series. Assuming that the Niño-3 SST in these control runs is statistically stationary and that the individual sections of the time series are nearly independent, then the extremes of these three curves make up a 75% confidence interval³ for time series of this length (100 yr). At interannual periods this interval is fairly wide, even for century-long time series. Thus subtle changes in the models' ENSO spectra, as might arise in climate change simulations, may be difficult to distinguish without numerous ensemble members.

Yet even with time series of this length, it is easy to

² As the models are subjected to fixed 1990 radiative forcings, the latter observational period (1982–2004) is perhaps the more appropriate one for comparison with the simulations.

³ Select three values x_1, x_2, x_3 at random from a distribution with median θ . Then $P\{x_1, x_2, x_3 < \theta\} = P\{\theta < x_1, x_2, x_3\} = 0.5^3$. Thus the probability that θ lies between the extremes of x_1, x_2, x_3 is $1 - 2 \times 0.5^3 = 0.75$.

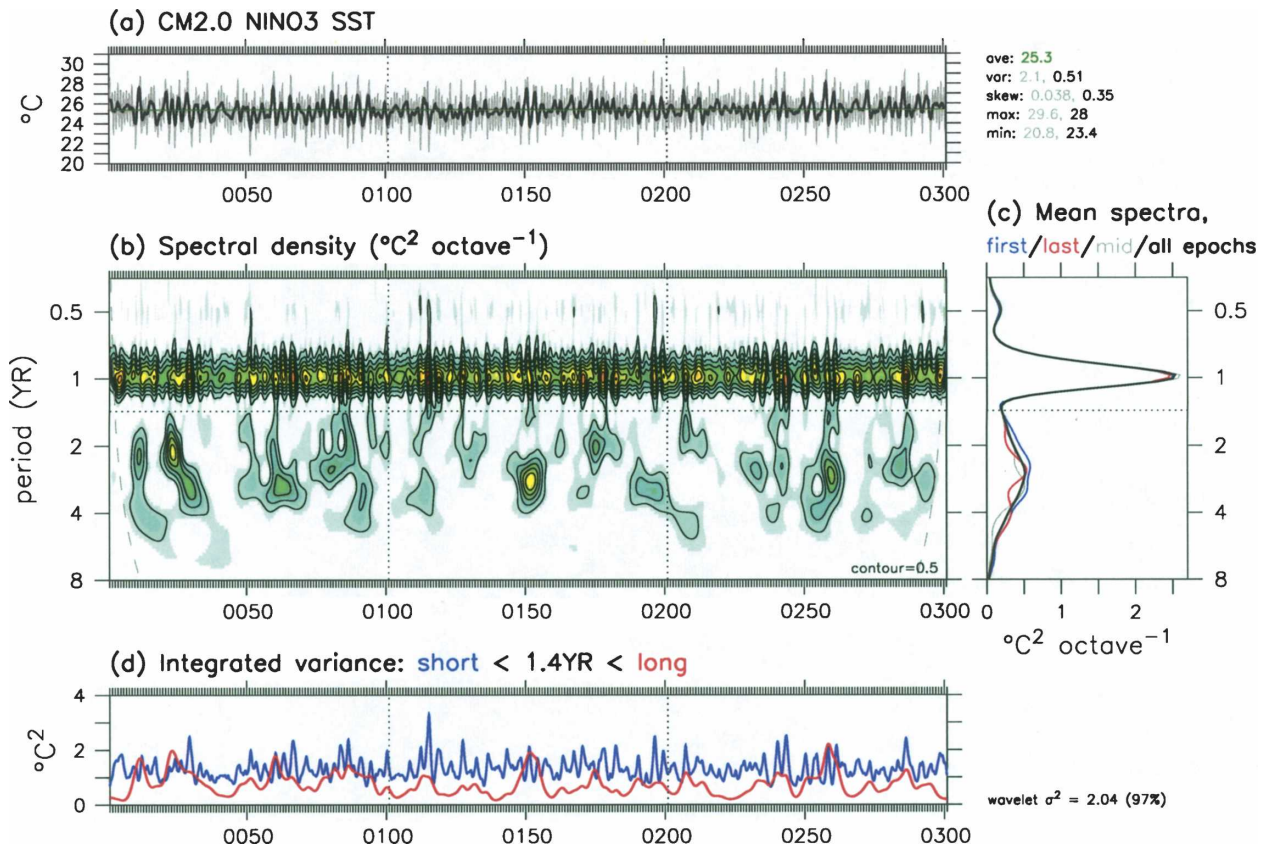


FIG. 20. (a) Time series of Niño-3-averaged SST as simulated by CM2.0. Gray line indicates monthly values, black line is a running annual mean, and green line is the 300-yr mean. The mean, variance, skewness, maximum, and minimum of each time series are listed to the right. (b) Spectral power density of the time series, obtained by convolution with a Morlet wavenumber-6 wavelet. The base contour line and contour interval are $0.5^{\circ}\text{C}^2 \text{ octave}^{-1}$, with shading incremented every half contour. The curved dashed line (cone of influence) represents twice the e -folding time for the wavelet response to a spike in the time series; below this line the spectral density is underestimated due to edge effects. (c) Time-averaged spectra for the entire time series (thick black), first third (thin blue), middle third (thin gray), and last third (thin red). (d) Running variance in the 0–1.4-yr spectral band (blue) and the 1.4–8-yr band (red). The total reconstructed wavelet variance and percent variance captured by the wavelet analysis are shown to the right.

distinguish among the ENSO spectra of the models and observations. At nearly all of the displayed time scales, the three spectral estimates from each simulation do not overlap (Fig. 19).⁴ Thus compared to ER.v2 the

simulated ENSOs are clearly too active, and compared to CM2.0, CM2.1 shows an even stronger ENSO that is shifted toward longer time scales.

c. Skewness

The skewness statistics for the monthly mean and annual-mean Niño-3 SSTs are shown to the right of Figs. 20a and 21a. As in observations, both models show a pronounced positive skewness of the interannual SSTs, with long, mild cold periods punctuated by short, extreme warm episodes.⁵ Many other CGCMs

⁴ Select six observations at random from a particular distribution. There are $\binom{6}{3} = 20$ ways to choose a set of three observations from among the six available ranks, but only one of these sets contains the three highest ranks. Thus the probability that the first three observations are larger than the second three is 20^{-1} . So given independent spectral estimates drawn from the same distribution, the probability that one set of three independent estimates exceeds the next three is 5%. The probability that one set would “exceed, or be exceeded by” another set is twice this (10%). Thus at each time scale where the two sets of three estimates do not overlap, the spectra are statistically distinct to at least 95% confidence for a one-tailed test, and at least 90% confidence for a two-tailed test.

⁵ The skewness of the monthly mean (annual-mean) observed Niño-3 SSTs is 0.05 (0.47) for ER.v2 1880–2004, and 0.27 (0.85) for OI.v2 1982–2004.

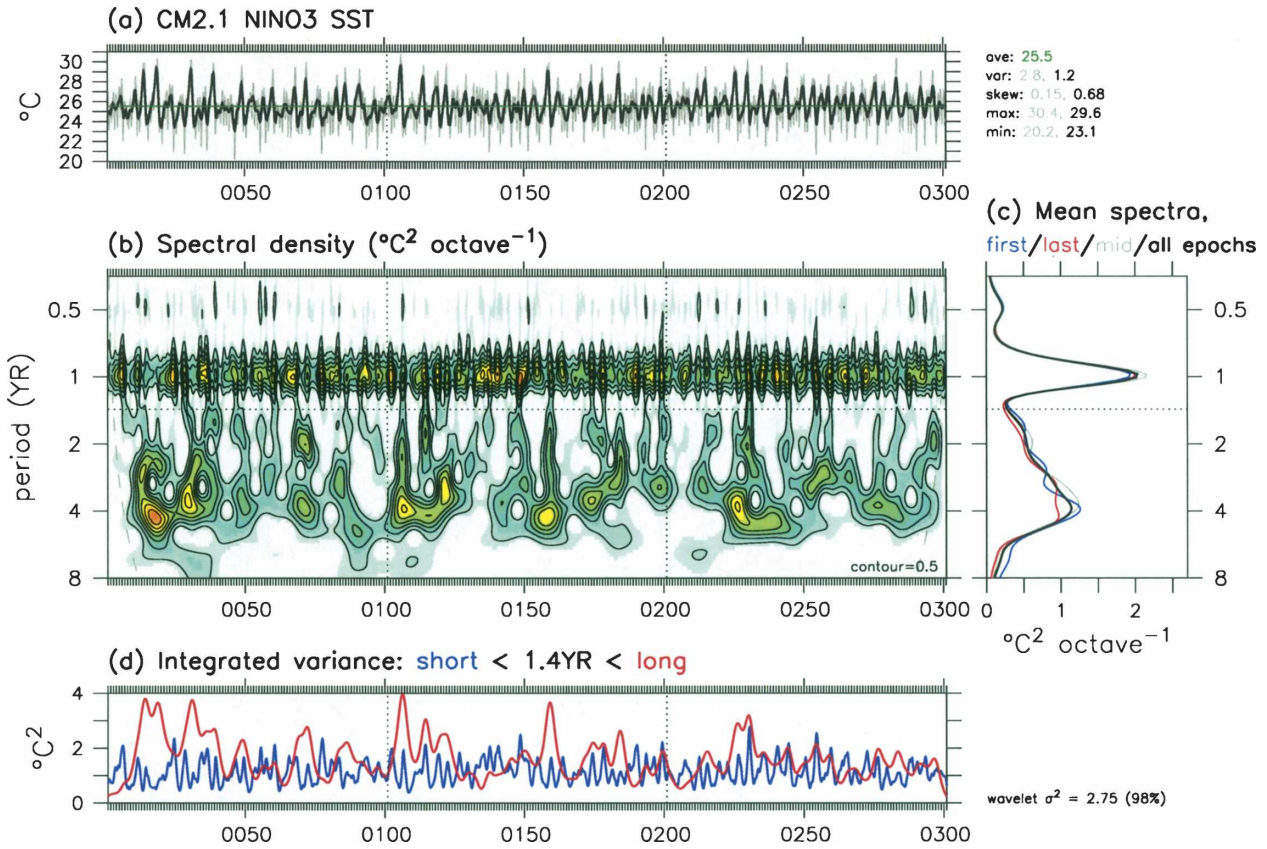


FIG. 21. Same as in Fig. 20, but for CM2.1.

substantially underestimate this skewness (Hannachi et al. 2003).

The enhanced skewness in CM2.1 compared to CM2.0 is probably tied to the eastward shift of the precipitation and τ'_x responses (Figs. 15 and 16), which brings nonlinear coupled feedbacks into play in the eastern Pacific. Warm events shift west Pacific convection eastward, generating stress anomalies where they can most effectively couple with the shallow oceanic thermocline via local upwelling. Cold events, on the other hand, shift convection westward, generating only weak air–sea feedbacks in the eastern Pacific.

d. Seasonal phase locking

Figure 22 shows the variance of interannual Niño-3 SST anomalies as a function of calendar month. The observed Niño-3 SSTAs tend to peak near the end of the calendar year, with a variance maximum in November and a minimum in boreal spring. While the models do show a spring variance minimum, and a broad peak from August through February, the seasonal phase locking is not as strong and sharp as in the observations. A monthly histogram of moderate-to-large Niño-3 SSTA peaks (not shown) indicates that simulated

events tend to peak either in July–August or in January–February. This semiannual locking of the model ENSOs is likely tied to the semiannual cycle of the background convection and currents in the eastern Pa-

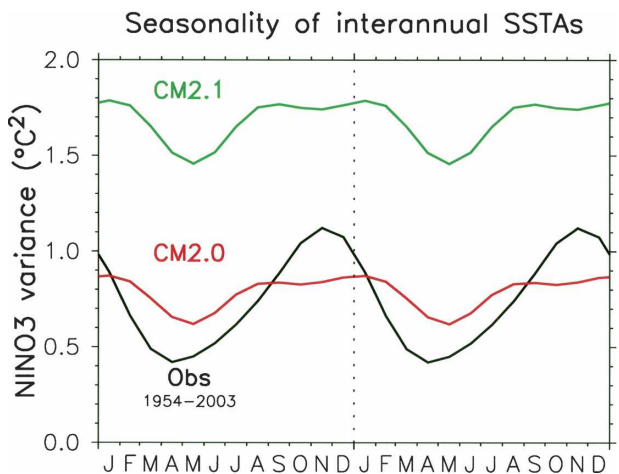


FIG. 22. Seasonality of the interannual variance of Niño-3-averaged SSTAs, from observations, CM2.0, and CM2.1. The SSTAs are filtered as in Fig. 14 prior to computing the variance. The horizontal axis spans two calendar cycles from Jan through Dec. Observations correspond to the ER.v2 analysis.

Lag-regressions onto NINO3 SSTA

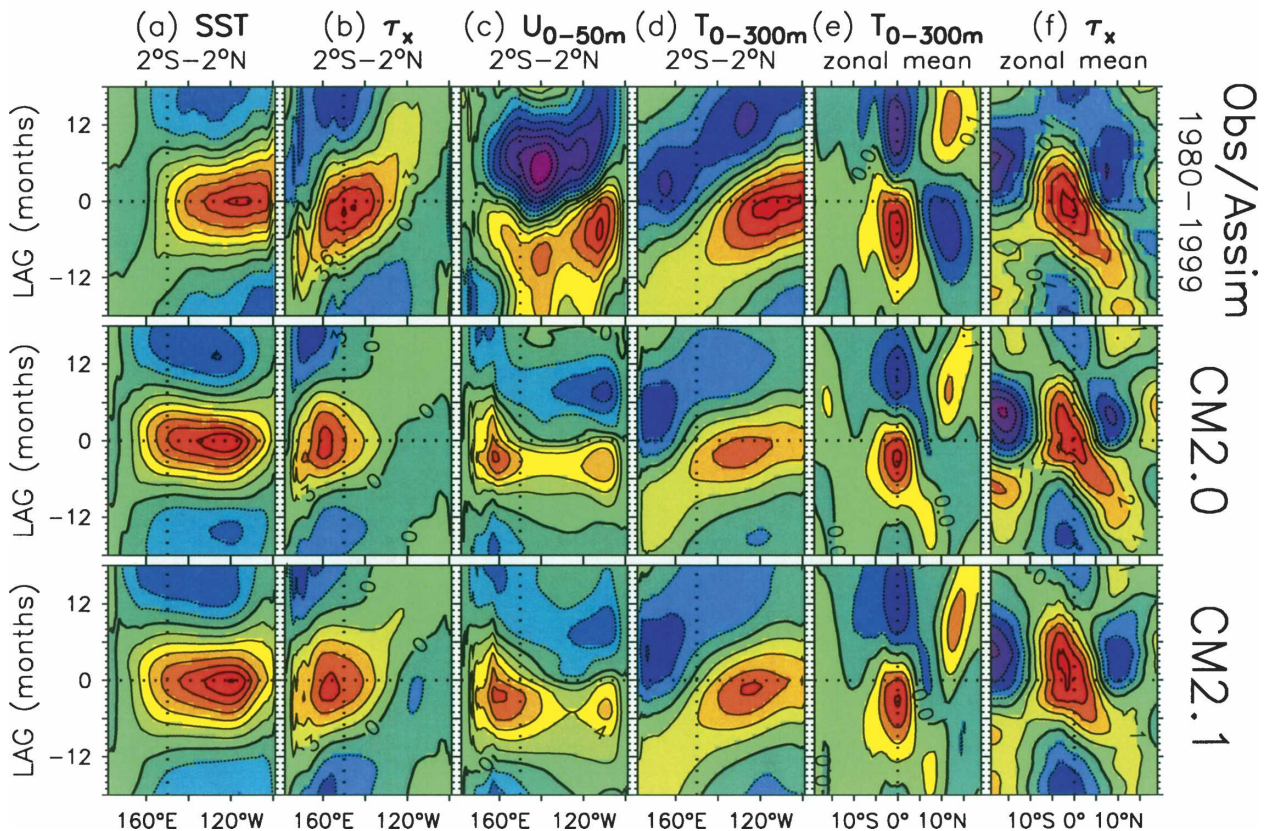


FIG. 23. Lag regressions onto Niño-3-averaged SST anomalies. Time flows upward and spans a period of 36 months. Lag-0 (horizontal dotted line) indicates the Niño-3 SSTA peak; positive lags correspond to the variable lagging Niño-3 SSTAs in time, negative lags to the variable leading Niño-3 SSTAs in time. Columns correspond to regressions for (a) SST (by 0.2) averaged over 2°S – 2°N , (b) zonal wind stress (by $3 \text{ mPa}^{\circ}\text{C}^{-1}$) averaged over 2°S – 2°N , (c) zonal currents (by $2 \text{ cm s}^{-1}\text{C}^{-1}$) averaged over 2°S – 2°N over the top 50 m of the ocean, (d) temperature (by 0.2) averaged over 2°S – 2°N over the top 300 m of the ocean, (e) temperature (by 0.1) averaged zonally across the Pacific over the top 300 m of the ocean, and (f) zonal wind stress (by $1 \text{ mPa}^{\circ}\text{C}^{-1}$) averaged zonally across the Pacific. First row corresponds to years 1980–99 from ER.v2 for SST, from ERA-40 for τ_x^z , and from the GFDL/ARCs ocean analysis for the currents and subsurface temperatures. Second and third rows correspond to the CM2.0 and CM2.1 simulations, respectively.

cific, associated with double ITCZ and the seasonal reversal of the meridional SST gradient and winds in the east (Figs. 3, 11, 12, and 13).

e. Evolution and mechanism

Figure 23 shows the average evolution of ENSO, based on a set of Niño-3 SSTA lag regressions⁶ for the models and for the GFDL/ARCs ocean analysis. The observational analysis for 1980–99 shows a nearly stationary growth of equatorial SSTAs from the coast of South America to 160°E (Fig. 23a). The observed

SSTAs develop slightly earlier in the west than in the east (both about 9–12 months prior to the event peak) and then decay eastward about 9–12 months after the peak.⁷ At the Niño-3 SSTA peak there are cold anomalies in the far western Pacific. There are also cold SSTAs in the central Pacific both before and after the warm event.

In the western and central Pacific, both models show the observed slightly westward-propagating cooling signature following the demise of the warm event (at 12-month lag), but show a subsequent cooling that is too

⁶ Although these regressions include cold events as well, for simplicity we shall describe the ENSO evolution in terms of a warm event.

⁷ Note that there is some variation in the observed SSTA propagation associated with ENSO. In particular, the observed equatorial SSTAs show a greater tendency toward westward propagation before 1980 than afterward (Wang 1995; Wang and An 2002).

strong and is shifted slightly west of the observations. East of 120°W, CM2.0 shows less eastward propagation than observed for 1980–99, while CM2.1 captures this feature somewhat better.

In Fig. 23b, the observed equatorial zonal wind stress anomalies show a pronounced eastward-moving signature in the west–central Pacific, with precursor westerlies in the west evident up to 12 months prior to the Niño-3 SSTA peak. The observed peak westerly anomalies occur near the date line, about one month before the Niño-3 SSTA peak, and at about the same time easterly anomalies begin developing in the far west. While CM2.0 and CM2.1 both show an eastward-moving signature in τ'_x , strong westerly anomalies do not propagate as far out into the Pacific basin as in the observations (CM2.1 shows some improvement over CM2.0 in this regard). Although the peak τ'_x is weak in the models, the zonal extent of the westerly anomalies is slightly broader than observed—since at the event peak the models have westerly anomalies in the far west Pacific instead of weak easterly anomalies as observed. CM2.1 gives a stronger τ'_x response than CM2.0, with both stronger westerlies in the western–central Pacific and stronger easterlies in the far eastern Pacific at the event peak.

As shown in Fig. 23c, the near-surface equatorial zonal currents in the observational assimilation lead the Niño-3 SST, with eastward currents peaking in the east Pacific about 3–9 months before the warm peak, and westward currents developing in the central and eastern Pacific at the warm peak and for the subsequent several months. Weak eastward currents are evident in the far west throughout the warm phase. The amplitude and phase of the zonal current anomalies are important, because they help transition the Pacific between warm and cold events by advecting on the strong background zonal SST gradient (Picaut et al. 1997; Jin and An 1999). Prior to the warming, eastward advection of the warm pool helps to warm the east; and after the event, westward advection of the cold tongue helps to restore the Pacific back toward equilibrium, often with an overshoot into a cold event. The models reproduce these features qualitatively, although the details are different. Both CM2.0 and CM2.1 show eastward current anomalies all along the equator up to 10 months prior to the warm peak (although these eastward current anomalies are somewhat weaker, and shifted farther westward, than in the analysis). The models also capture the observed reversal of these anomalies during the ENSO event, but the subsequent westward anomalies in the central basin following the event peak are too weak, and shifted farther east than in the analysis. That CM2.0 has stronger zonal current anomalies than

CM2.1 in the central and eastern Pacific is likely tied to the narrower meridional structure of its τ'_x response (Fig. 16; Wittenberg 2002) and may partly explain its shorter ENSO period compared to CM2.1 (see section 5b).

In the assimilation, there is a slow eastward propagation of equatorial heat content anomalies (Fig. 23d), with a reduction of the zonal slope of the thermocline at the peak of El Niño. The models show similar features, although with weaker amplitude and a westward shift. This weaker thermocline variability is directly tied to the weak and westward-shifted τ'_x in the models (Fig. 16).

Figure 23e shows a decrease in zonal-average heat content at the equator during El Niño, which occurs in the models as well as in the observational analysis. The equatorial heat content peaks 3–4 months prior to the peak Niño-3 SSTAs, at the same time that there is a deficit of heat content along 5°–10°N. As the warm event peaks and then begins to decay, increased evaporation and decreased insolation cool the surface, and anomalous poleward currents discharge heat from the equator. (Vertical heat fluxes across 300-m depth are quite small.) One year after the event peak, there is a deficit of heat content on the equator and positive heat content anomalies along 7°–15°N. Like the equatorial zonal current anomalies, the recharge/discharge of equatorial heat content is an important transitioner for ENSO (Jin 1997a). That the recharge/discharge of equatorial heat content is stronger in CM2.0 than in CM2.1 may partly contribute to the shorter period in that model compared to CM2.1.

Lag regressions for the subsurface anomalies were also computed for the NCEP ODA (not shown). The evolution of subsurface anomalies in that analysis is similar to GFDL/ARCs (Fig. 23, first row), although the temperature and current anomalies in the east are weaker, and those in the west are stronger. The NCEP ODA also shows much weaker eastward zonal current anomalies in the central equatorial Pacific prior to the event peak.

Figure 23f indicates that one year prior to the warm peak, there is a near-equatorial anticyclonic curl associated with the zonal-mean τ'_x field, in both the observations and the models. On interannual time scales, this anticyclonic curl generates an equatorward transport in the upper ocean, which contributes to the equatorial recharge of heat content seen before the event in Fig. 23e. During and after the event peak, the zonal-mean curl changes sign, becoming cyclonic on both sides of the equator and subsequently contributing to the discharge of heat content from the equator.

In both models and observations, Fig. 23f shows a distinct southward progression of the westerly τ'_x through the warm event. This southeastward shift is a

common feature in the observations during the boreal winter of El Niño years and is associated with a weakening of the equatorial τ'_x as the zone of strong westerly anomalies moves south of the equator toward the warmest SSTs. The wind shift, and the resulting shoaling of the thermocline in the eastern equatorial Pacific, may play key roles in the timing of event termination (Lengaigne et al. 2006; Vecchi and Harrison 2006; Vecchi 2006).

6. ENSO teleconnections

a. Extratropical 200-hPa height field

The anomalous circulation associated with ENSO during the December–February (DJF) season is illustrated by the patterns of regression coefficients of 200-hPa height versus standardized Niño-3 SSTAs (Fig. 24). These regression charts display the typical pattern and amplitude of 200-hPa height variations corresponding to a one-standard-deviation change in the Niño-3 index.

The observed distribution in Fig. 24a shows a familiar wave train, with two high centers located over the subtropical eastern Pacific and over Canada, and two low centers over in the eastern extratropical North Pacific and the southern United States. This teleconnection pattern has been documented in detail by Horel and Wallace (1981) and others. The simulated amplitudes of the North Pacific and Canadian anomalies are weaker than the observed estimates by 20%–30%. There is also a westward displacement (by 20°–30° of longitude) of the North Pacific, Canadian, and southern U.S. centers in both CM2 simulations relative to the observed sites. In CM2.1, the low over the southern United States is no longer a distinct center, having merged with the low over the eastern extratropical North Pacific.

The westward shift of the simulated 200-hPa height anomalies is likely tied to the excessive westward spread of the SST anomalies and associated precipitation changes during the simulated ENSO events (section 5; Figs. 14, 15, and 25). The corresponding patterns generated by subjecting the atmospheric component of CM2.0 to observed SST forcing exhibit noticeably less model bias in the positions of the anomaly centers (Fig. 14 of GAMDT-04). It is also noteworthy that in the atmosphere-only simulation, the extratropical wave train for the 1957–58 event (when the peak SSTA was located near 150°–180°W) was displaced well to the west of the corresponding feature for the 1997–98 event (when the peak SSTA occurred near the South American coast, 90°–120°W). In both observed and simulated atmospheres, such longitudinal shifts in the wave trains strongly affect the interevent variability of the patterns

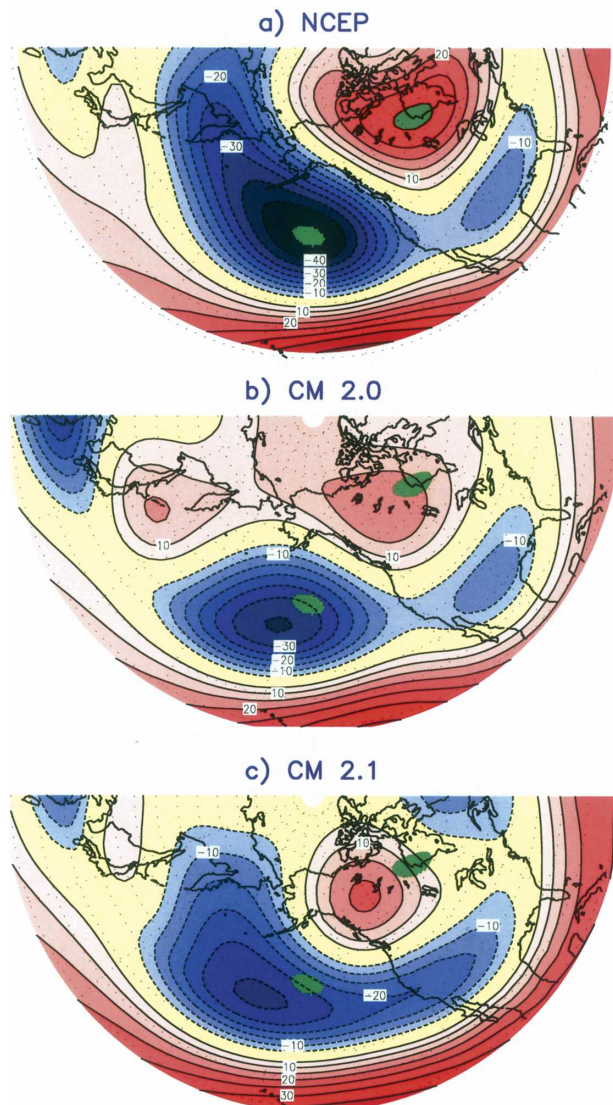


FIG. 24. Regressions of 200-hPa heights onto standardized Niño-3 SSTAs for the DJF season, computed using (a) NCEP1 reanalysis for 1951–2000, (b) CM2.0, and (c) CM2.1. Contour interval is 5 m, and the zero contour is not plotted. Green shading in all panels indicates the positions of the NCEP1 extrema over the North Pacific and Canada.

of temperature and precipitation changes over North America (Hoerling and Kumar 2002).

b. Precipitation field

Seasonal correlations between precipitation and Niño-3 SSTAs are displayed in Fig. 25. The CM2.0 results (not shown) are similar to those for CM2.1. Use of the correlation (as opposed to regression) coefficients is intended to more clearly reveal the precipitation features in the subtropics and midlatitudes, where the precipitation anomalies are weaker than those in the deep Tropics.

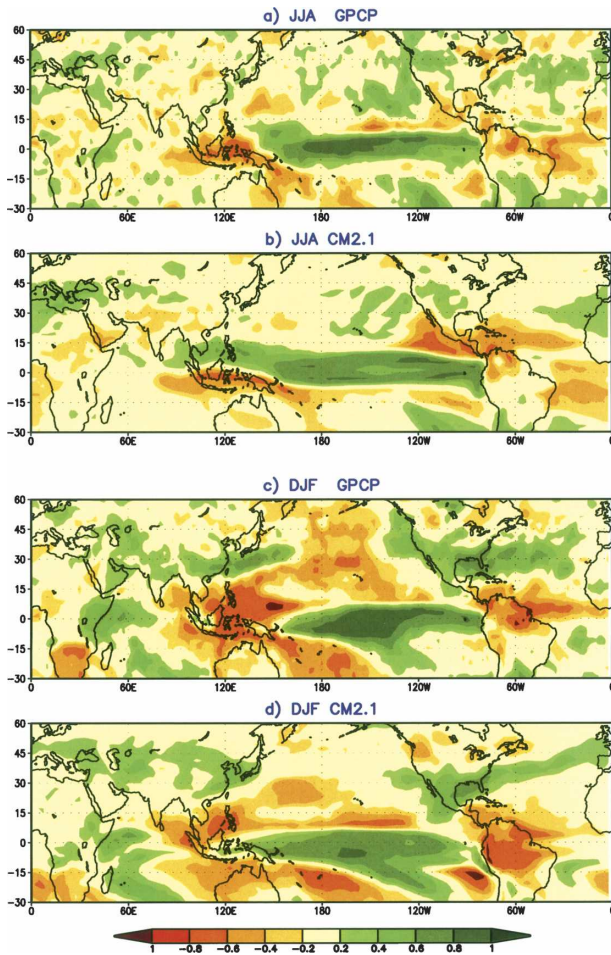


FIG. 25. Correlations of precipitation with Niño-3 SSTs for (a), (b) JJA and (c), (d) DJF, computed using (a), (c) observational estimates from GPCP.v2 for 1979–2000, and (b), (d) output from CM2.1. Green (brown) shading highlights wet (dry) anomalies with absolute correlation values exceeding 0.2, which corresponds to a significance level of 95% for the model data.

As noted in GAMDT-04 and section 5, the simulated positive precipitation anomaly in the equatorial Pacific extends too far west to the Indonesian Archipelago during warm events in both seasons (Figs. 25b,d); whereas the corresponding observations (Figs. 25a,c) indicate much drier conditions over Indonesia, as well as over the South China and Philippine Seas.

During the June–August (JJA) season, both model and observations (Figs. 25a,b) show dry anomalies over Central America and the surrounding waters, as well as the equatorial Atlantic and the northern part of South America. There is also some weaker indication of suppressed rainfall over parts of the south Asian monsoon regions during warm ENSO events.

Figures 25c,d show that in DJF, the model agrees well with observations regarding the northeastward

shift of the SPCZ rainfall during warm ENSO events. The dry conditions over the Bay of Bengal, South China Sea, western Indonesia, northern Australia, equatorial South America, and southern Africa are also captured by the model, as is the above-normal precipitation over southeastern China and the East China Sea, eastern equatorial Africa, and a broad belt extending eastward from the U.S. western seaboard across northern Mexico to the Gulf Coast and subtropical Atlantic. The precipitation features over east Asia are related to the anomalous near-surface anticyclone centered near the Philippine Sea during warm ENSO events (Wang et al. 2000). The enhanced precipitation over the southern part of North America and the surrounding maritime areas is associated with the higher frequency of synoptic-scale disturbances traveling along the deepened stationary trough over that region (Fig. 24).

7. Discussion

CM2.0 and CM2.1 represent substantial progress toward improved simulation of the tropical Pacific climatology, annual cycle, and ENSO. Most of the observed features are captured quite well, and these models should serve as excellent tools for understanding and predicting climate variations, and for investigating the response of the climate system to external forcings. Some problems do remain, many of which are shared with other CGCMs. The following are some key targets for future coupled model development efforts.

a. Meridional asymmetry of the background state

One problem in the models is a lack of sufficient meridional asymmetry in the annual-mean state of the tropical Pacific. This is most evident in the east, which exhibits a warm bias and a double ITCZ south of the equator, weak cross-equatorial southerly winds, an underestimate of low cloudiness near the South American coast, and a weak meridional shear of the surface zonal currents ($\partial_y u$) north of the equator. This “symmetry bias” is evident below the ocean’s surface as well, where the thermocline is meridionally too flat.

The weak simulated north–south asymmetry affects the seasonal cycle, giving rise to an unrealistic annually reversing meridional SST gradient and τ_y in the east that generate a semiannual cycle in the near-equatorial wind speed, evaporation, and upwelling. These may also contribute to a stronger-than-observed semiannual component in the simulated equatorial SST, τ_x , surface currents, and EUC.

The meridional symmetry in the models, and the lack of strong southerlies and low cloudiness near the Peru

coast, may also be linked to the warm SST and strong near-surface stratification at the coast—which along with the weak coastal upwelling could reduce the connection between the subsurface thermocline variability and the coastal SST. This may further limit SSTA variability near the coast during ENSO, and bring about a further westward shift of this variability relative to observations. Preliminary CGCM experiments at GFDL in which the atmospheric horizontal resolution has been doubled have shown some promising results, nearly eliminating the mean SST warm bias near the Peru coast. Presumably this is due to the more realistic representation of the abrupt topography of the Andes Mountains, as well as better resolution of the coastal atmospheric dynamics. It remains to be seen whether these improved coastal SSTs will also improve the coupled simulation away from the Peru coast.

The weak meridional asymmetry of CM2.0 and CM2.1 may also be preventing the annual phase locking of the simulated ENSO events. Both the westerly wind bursts that help to initiate ENSO events and the shifts in τ'_x and upwelling that help to terminate them depend on an annual cycle of convection that is strongly controlled by meridionally asymmetric SST variations. Even the simulated zonal shifts in convection appear to be affected by the symmetry bias in SST: model precipitation anomalies tend to spread eastward both north and south of the equator, instead of mostly in the north as observed.

Improving the simulated meridional asymmetry is a difficult challenge and may require a number of improvements in the atmospheric models—including better representation of low clouds and their radiative properties near the Peru Coast, improved boundary layer parameterization in the subsidence regime of the east Pacific, and a more sophisticated convection scheme to better represent the ITCZ and its seasonal migration. The ocean models may be partly to blame as well, since they too show a symmetry bias when driven by observational estimates of the surface heat and momentum fluxes.

b. Cold equator and westward-shifted convection

A second key problem is the equatorial SST cold bias, which appears to keep atmospheric convection and westerly wind anomalies from migrating far enough eastward during El Niño events. As a result, many of the background fields (Figs. 1, 3, 4, and 7) and ENSO patterns (Figs. 14–18) are displaced west of the observations. When the convection does move east during strong warm events, it still tends to avoid the cold equator, instead moving eastward along the zones of warmest SST at 5°S and 5°N.

A lack of sufficient meridional shear in the background τ_x and zonal currents in the northeastern equatorial Pacific (Figs. 4 and 7), in tandem with the difficulty in parameterizing the ocean viscosity in this region, may be responsible for the weak TIW variability simulated in CM2.0 and CM2.1. TIWs can transport large amounts of heat meridionally, vertically, and through the air–sea interface (Stockdale et al. 1998; Jochum et al. 2005), which may both warm and widen the equatorial cold tongue in the real world. The TIWs may also affect the skewness of the simulated seasonal and ENSO SSTs, since the TIWs are generally strongest during boreal autumn and La Niña when the cold tongue is enhanced.

Another challenge at the current resolution of the ocean model is representing the deep, narrow channels and sills of the Indonesian straits. Errors in the volume transport and vertical structure of the Indonesian throughflow (ITF), when coupled with intense air–sea feedbacks over the Indo-Pacific, can substantially alter the simulated thermal structure of these basins. Indeed, a CM2.1 experiment in which the ITF is blocked between Lombok and New Guinea induces a permanent, El Niño–like warming of over 0.5°C in the eastern equatorial Pacific (Q. Song 2005, personal communication). Sustained, dense, high-quality observations and high-resolution modeling of ITF properties may therefore be key for improving CGCMs.

The mean rainfall in the far west Pacific seems pegged to New Guinea—which may indicate problems representing the topography or the heat and moisture fluxes over the island's land surface. The convection may also be tracking the models' SST hot spots, which also tend to sit near the New Guinea coast (Fig. 1). It will be important to improve the mean position of the west Pacific convection in the models, so that intraseasonal variability (such as the Madden–Julian oscillation and westerly wind bursts), and their impacts on ENSO, can be properly represented.

c. ENSO surface flux patterns

As was the case for the annual-mean fields in section 3, the errors in the coupled model ENSO regression patterns appear to arise mostly from errors in the simulated climatological SSTs—especially the equatorial cold bias that inhibits the eastward shift of convection during warm events. When the component atmospheric GCMs are driven by observed SSTs, the precipitation, wind stress, and heat flux anomaly patterns agree much better with observations (GAMDT-04; Sun et al. 2006). Yet even in this SST-driven context the atmosphere models exhibit hints of the CGCM biases—including a faint double ITCZ in the east along 5° S, too much

shortwave radiation absorbed by the ocean along the coast of South America, and ENSO precipitation anomalies that are shifted slightly too far west along the equator.

One possible cause for the excessive ENSO amplitude is the lack of a sufficient surface heat flux damping of SSTAs in the models (Figs. 17 and 18). Indeed, this damping is even weaker in CM2.1 than in CM2.0. Studies in a hierarchy of models (Zebiak and Cane 1987; Battisti and Hirst 1989; Wang and Weisberg 1996; Jin 1997a,b; Wittenberg 2002) have shown that reducing this heat flux damping tends to destabilize and amplify ENSO. A key challenge for the observational community will be to narrow the uncertainties associated with the air–sea fluxes of heat, momentum, and water to provide more reliable forcings and more stringent validation datasets for climate modelers. For the solar and latent surface heat fluxes, however, the simulations clearly lie outside the range of available observational estimates—so some improvement in the model fluxes is warranted.

The differences in ENSO between CM2.0 and CM2.1 can also be connected to the differences in wind stress coupling (Fig. 16). Studies with intermediate models (An 2000; An and Wang 2000; Wang and An 2002; Wittenberg 2002) and a hybrid CGCM (Harrison et al. 2002) have demonstrated that shifting the τ'_x response eastward tends to increase the amplitude and period of ENSO, by enhancing positive air–sea feedbacks in the eastern Pacific and delaying the negative feedbacks associated with the slow adjustment of the equatorial thermocline. Other work (Kirtman 1997; An and Wang 2000; Wittenberg 2002) has described the sensitivity of ENSO to the meridional shape of the τ'_x response. A meridionally wider τ'_x response generates less wind stress curl close to the equator, weakening the delayed negative feedback associated with the slow adjustment of the zonal-mean thermocline depth, giving a stronger ENSO with a longer period. Increasing the zonally integrated strength of the wind stress feedback also tends to strengthen ENSO in realistic regimes (Zebiak and Cane 1987; Neelin 1991; Wakata and Sarachik 1994; Neelin et al. 1998). Thus the three differences between the models' wind stress responses—the eastward shift, the meridional widening, and the strengthening of the τ'_x response in CM2.1 relative to CM2.0—all appear to be consistent with the increased ENSO amplitude and period in CM2.1. Careful experiments will be needed to determine which effects dominate in these models.

8. Conclusions

We have described multicentury control runs from the GFDL global coupled ocean–atmosphere–land–ice

models, CM2.0 and CM2.1, in terms of their tropical Pacific climate, seasonal cycle, ENSO variability, and ENSO teleconnections. We conclude that substantial progress has been made toward realistic simulation of these features, though some challenges remain.

- 1) Most of the key features of the observed climate and variability of tropical Pacific SST, trade winds and precipitation, surface heat fluxes, surface currents, Equatorial Undercurrent, and subsurface thermal structure are well captured by the models.
- 2) Annual-mean SST biases in the control simulations include a warm bias along the coast of South America, a modest cold bias along the equator, and a slight warm bias in the vicinity of the ITCZ.
- 3) The simulated annual-mean surface fluxes of water, heat, and momentum are in reasonable agreement with observations. Problems include a dry bias at the equator with too much insolation over the central and eastern Pacific; excessive precipitation south of the equator in the east Pacific; a westward shift of the trade winds resulting in too much evaporation west of the date line; and weaker-than-observed southerly winds with too little evaporation near the coast of South America.
- 4) The simulated equatorial annual-mean subsurface temperatures are quite realistic at the equator, with the thermocline at approximately the right depth. However, the thermocline is too diffuse in the vertical and shows a slightly stronger zonal slope than in observations, with strong near-surface stratification along the coast of South America. The simulated zonal-mean annual-mean thermocline is meridionally too flat.
- 5) The annual-mean EUC is well simulated. The mean surface current patterns, however, are shifted 20°–30° west of those observed, and the SEC and NECC are too weak in the eastern Pacific. The simulated TIWs are also weaker than observed.
- 6) The simulations show a robust, westward-propagating annual cycle of SST and zonal winds along the equator, which is in good qualitative agreement with observations. An overly strong semiannual component of the zonal winds, however, generates a similar semiannual signal in the equatorial zonal currents. In the eastern Pacific, the off-equatorial annual cycle is too strong—in boreal spring, excessive SSTs and rainfall south of the equator contribute to an unrealistic reversal of the equatorial meridional winds.
- 7) The models have a robust ENSO with multidecadal fluctuations in amplitude, an irregular period between 2 and 5 yr, and SST anomalies that are

skewed toward warm events as observed. The evolution of ENSO subsurface temperatures is quite realistic, as are the ENSO correlations with precipitation anomalies outside the tropical Pacific. However, the simulated ENSOs are too strong, too weakly damped by surface heat fluxes, and are not sufficiently phase locked to the end of the calendar year. The simulated ENSO patterns of SST, wind stress, and precipitation variability are shifted 20°–30° west of the observed patterns. Such problems appear to be linked to the model mean state biases—namely the equatorial cold bias, the double ITCZ, and the overstratified surface waters near the South American coast.

- 8) Relative to observations, the models show a 20°–30° westward shift of the ENSO teleconnections to Northern Hemisphere 200-hPa heights during winter, related to the westward shift of the ENSO tropical rainfall anomalies.
- 9) By several measures, CM2.0 outperforms CM2.1 in the tropical Pacific, with reduced SST biases near the equator and the South American coast, more realistic surface insolation at the equator, reduced off-equatorial subsurface temperature biases, a less intense double ITCZ, stronger annual-mean surface currents, a more realistic annual cycle, and a less intense ENSO. CM2.1, on the other hand, shows a reduced warm bias below the equatorial thermocline, reduced precipitation biases in the SPCZ and northern ITCZ, a longer-period ENSO with less westward displacement of the variability relative to observations, and a strong skewness of ENSO SST anomalies toward warm events as observed.

Acknowledgments. Tom Knutson, Gabriel Vecchi, Ron Stouffer, Steve Klein, Tony Gordon, and three anonymous reviewers provided insightful comments that greatly improved this paper. The authors thank the providers of all of the observational datasets listed in Table 1. We also thank the members of GFDL Modeling Services for their assistance with model infrastructure support and data processing. Wavelet analyses were produced using Fortran codes provided by C. Torrence and G. Compo at <http://paos.colorado.edu/research/wavelets>.

REFERENCES

- AchutaRao, K., and K. R. Sperber, 2002: Simulation of the El Niño Southern Oscillation: Results from the Coupled Model Intercomparison Project. *Climate Dyn.*, **19**, 191–209.
- , —, and the CMIP Modeling Groups, 2000: El Niño Southern Oscillation in coupled GCMs. PCMDI Rep. 61, PCMDI, LLNL, University of California, Livermore, CA, 46 pp.
- Adler, R. F., and Coauthors, 2003: The Version-2 Global Precipitation Climatology Project (GPCP) Monthly Precipitation Analysis (1979–present). *J. Hydrometeorol.*, **4**, 1147–1167.
- Alexander, M. A., I. Blade, M. Newman, J. R. Lanzante, N.-C. Lau, and J. D. Scott, 2002: The atmospheric bridge: The influence of ENSO teleconnections on air–sea interaction over the global oceans. *J. Climate*, **15**, 2205–2231.
- An, S.-I., 2000: On the slow mode of a simple air–sea coupled model: The sensitivity to the zonal phase difference between the SST and the atmospheric heating. *J. Meteor. Soc. Japan*, **78**, 159–165.
- , and B. Wang, 2000: Interdecadal change of the structure of the ENSO mode and its impact on the ENSO frequency. *J. Climate*, **13**, 2044–2055.
- Atlas, R., R. N. Hoffman, S. C. Bloom, J. C. Jusem, and J. Ardizzone, 1996: A multiyear global surface wind velocity dataset using SSM/I wind observations. *Bull. Amer. Meteor. Soc.*, **77**, 869–882.
- Barnett, T. P., M. Latif, E. Kirk, and E. Roeckner, 1991: On ENSO physics. *J. Climate*, **4**, 487–515.
- Barsugli, J. J., and P. D. Sardeshmukh, 2002: Global atmospheric sensitivity to tropical SST anomalies throughout the Indo-Pacific basin. *J. Climate*, **15**, 3427–3442.
- Battisti, D. S., and A. C. Hirst, 1989: Interannual variability in a tropical atmosphere–ocean model: Influence of the basic state, ocean geometry and nonlinearity. *J. Atmos. Sci.*, **46**, 1687–1712.
- Behringer, D. W., M. Ji, and A. Leetmaa, 1998: An improved coupled model for ENSO prediction and implications for ocean initialization. Part I: The ocean data assimilation system. *Mon. Wea. Rev.*, **126**, 1013–1021.
- Bonjean, F., and G. S. E. Lagerloef, 2002: Diagnostic model and analysis of the surface currents in the tropical Pacific Ocean. *J. Phys. Oceanogr.*, **32**, 2938–2954.
- Bourassa, M. A., S. R. Smith, and J. J. O'Brien, 2001: A new FSU winds and flux climatology. Preprints, *11th Conf. on Interactions of the Sea and Atmosphere*, San Diego, CA, Amer. Meteor. Soc., 9–12.
- Cole, J., 2001: A slow dance for El Niño. *Science*, **291**, 1496–1497.
- da Silva, A. M., C. C. Young, and S. Levitus, 1994: *Algorithms and Procedures*. Vol. 1, *Atlas of Surface Marine Data*, NOAA Atlas NESDIS 6, 83 pp.
- Davey, M. K., M. Huddleston, K. R. Sperber, and the Model Data Contributors, 2000: STOIC: A study of coupled GCM climatology and variability in tropical ocean regions. STOIC Project Rep., CLIVAR-WGSIP, 41 pp.
- , —, —, and the Model Data Contributors, 2002: STOIC: A study of coupled model climatology and variability in tropical ocean regions. *Climate Dyn.*, **18**, 403–420.
- Delworth, T. L., and Coauthors, 2006: GFDL's CM2 global coupled climate models. Part I: Formulation and simulation characteristics. *J. Climate*, **19**, 643–674.
- Derber, J., and A. Rosati, 1989: A global oceanic data assimilation system. *J. Phys. Oceanogr.*, **19**, 1333–1347.
- Diaz, H. F., and V. Markgraf, Eds., 2000: *El Niño and the Southern Oscillation: Multiscale Variability and Its Impacts on Natural Ecosystems and Society*. Cambridge University Press, 496 pp.
- Dijkstra, H. A., and J. D. Neelin, 1995: Ocean–atmosphere interaction and the tropical climatology. Part II: Why the Pacific cold tongue is in the east. *J. Climate*, **8**, 1343–1359.
- Easterling, D. R., G. A. Meehl, C. Parmesan, S. A. Changnon,

- T. R. Karl, and L. O. Mearns, 2000: Climate extremes: Observations, modeling, and impacts. *Science*, **289**, 2068–2074.
- Fedorov, A. V., and S. G. Philander, 2000: Is El Niño changing? *Science*, **288**, 1997–2002.
- Gent, P. R., and J. C. McWilliams, 1990: Isopycnal mixing in ocean circulation models. *J. Phys. Oceanogr.*, **20**, 150–155.
- GFDL Global Atmospheric Model Development Team, 2004: The new GFDL global atmosphere and land model AM2/LM2: Evaluation with prescribed SST simulations. *J. Climate*, **17**, 4641–4673.
- Gnanadesikan, A., and Coauthors, 2006: GFDL's CM2 global coupled climate models. Part II: The baseline ocean simulation. *J. Climate*, **19**, 675–697.
- Goddard, L., S. J. Mason, S. E. Zebiak, C. F. Ropelewski, R. Basher, and M. A. Cane, 2001: Current approaches to seasonal to interannual climate predictions. *Int. J. Climatol.*, **21**, 1111–1152.
- Grassl, H., V. Jost, R. Kumar, J. Schulz, P. Bauer, and P. Schluesel, 2000: The Hamburg Ocean-Atmosphere Parameters and Fluxes from Satellite Data (HOAPS): A climatological atlas of satellite-derived air-sea-interaction parameters over the oceans. Tech. Rep. 312, Max Planck Institute for Meteorology, Hamburg, Germany, 130 pp.
- Greenwald, T. J., G. L. Stephens, and T. H. Vonder Haar, 1993: A physical retrieval of cloud liquid water over the global oceans using Special Sensor Microwave/Imager (SSM/I) observations. *J. Geophys. Res.*, **98**, 18 471–18 488.
- Griffies, S. M., 1998: The Gent–McWilliams skew flux. *J. Phys. Oceanogr.*, **28**, 831–841.
- , A. Gnanadesikan, R. C. Pacanowski, V. D. Larichev, J. K. Dukowicz, and R. D. Smith, 1998: Isonutral diffusion in a z-coordinate ocean model. *J. Phys. Oceanogr.*, **28**, 805–830.
- , and Coauthors, 2005: Formulation of an ocean model for global climate simulations. *Ocean Sci.*, **1**, 45–79.
- Grist, J. P., and S. A. Josey, 2003: Inverse analysis adjustment of the SOC air–sea flux climatology using ocean heat transport constraints. *J. Climate*, **16**, 3274–3295.
- Hahn, C. J., W. B. Rossow, and S. G. Warren, 2001: ISCCP cloud properties associated with standard cloud types identified in individual surface observations. *J. Climate*, **14**, 11–28.
- Hannachi, A., D. B. Stephenson, and K. R. Sperber, 2003: Probability-based methods for quantifying nonlinearity in the ENSO. *Climate Dyn.*, **20**, 241–256.
- Harrison, M. J., A. Rosati, B. J. Soden, E. Galanti, and E. Tziperman, 2002: An evaluation of air–sea flux products for ENSO simulation and prediction. *Mon. Wea. Rev.*, **130**, 723–732.
- Hoerling, M. P., and A. Kumar, 2002: Atmospheric response patterns associated with tropical forcing. *J. Climate*, **15**, 2184–2203.
- Horel, J. D., and J. M. Wallace, 1981: Planetary-scale atmospheric phenomena associated with the Southern Oscillation. *Mon. Wea. Rev.*, **109**, 813–829.
- Houghton, J. T., Y. Ding, D. J. Griggs, M. Noguer, P. J. van der Linden, X. Dai, K. Maskell, and C. A. Johnson, Eds., 2001: *Climate Change 2001: The Scientific Basis*. Cambridge University Press, 881 pp.
- Hsu, H.-H., and A. D. Moura, 2001: Workshop on the impacts of the 1997–99 ENSO. *Bull. Amer. Meteor. Soc.*, **82**, 305–312.
- IFREMER/CERSAT, 2002: QuikSCAT Scatterometer mean wind field products user manual. C2-MUT-W-04-IF, version 1.0, IFREMER/CERSAT, Plouzane, France, 47 pp.
- Jin, F.-F., 1997a: An equatorial ocean recharge paradigm for ENSO. Part I: Conceptual model. *J. Atmos. Sci.*, **54**, 811–829.
- , 1997b: An equatorial ocean recharge paradigm for ENSO. Part II: A stripped-down coupled model. *J. Atmos. Sci.*, **54**, 830–847.
- , and S.-I. An, 1999: Thermocline and zonal advective feedbacks within the equatorial ocean recharge oscillator model for ENSO. *Geophys. Res. Lett.*, **26**, 2989–2992.
- Jochum, M., R. Murtugudde, R. Ferrari, and P. Malanotte-Rizzoli, 2005: The impact of horizontal resolution on the tropical heat budget in an Atlantic Ocean model. *J. Climate*, **18**, 841–851.
- Josey, S. A., E. C. Kent, and P. K. Taylor, 1998: The Southampton Oceanography Centre (SOC) ocean–atmosphere heat, momentum and freshwater flux atlas. Tech. Rep. 6, Southampton Oceanography Centre, 30 pp.
- Kanamitsu, M., W. Ebisuzaki, J. Woollen, S.-K. Yang, J. J. Hnilo, M. Fiorino, and G. L. Potter, 2002: NCEP–DOE AMIP-II Reanalysis (R-2). *Bull. Amer. Meteor. Soc.*, **83**, 1631–1643.
- Kessler, W. S., L. M. Rothstein, and D. Chen, 1998: The annual cycle of SST in the eastern tropical Pacific, diagnosed in an ocean GCM. *J. Climate*, **11**, 777–799.
- Kirtman, B. P., 1997: Oceanic Rossby wave dynamics and the ENSO period in a coupled model. *J. Climate*, **10**, 1690–1704.
- Kistler, R., and Coauthors, 2001: The NCEP–NCAR 50-year reanalysis: Monthly means CD-ROM and documentation. *Bull. Amer. Meteor. Soc.*, **82**, 247–268.
- Kubota, M., N. Iwasaka, S. Kizu, M. Konda, and K. Kutsuwada, 2002: Japanese ocean flux data sets with use of remote sensing observations (J-OFURO). *J. Oceanogr.*, **58**, 213–225.
- Large, W. G., J. C. McWilliams, and S. C. Doney, 1994: Oceanic vertical mixing: A review and a model with a vertical K-profile boundary layer parameterization. *Rev. Geophys.*, **32**, 363–403.
- , G. Danabasoglu, J. C. McWilliams, P. R. Gent, and F. O. Bryan, 2001: Equatorial circulation of a global ocean climate model with anisotropic horizontal viscosity. *J. Phys. Oceanogr.*, **31**, 518–536.
- Latif, M., and Coauthors, 1998: A review of the predictability and prediction of ENSO. *J. Geophys. Res.*, **103**, 14 375–14 393.
- , K. Sperber, and CMIP Participants, 2001: ENSIP: The El Niño Simulation Intercomparison Project. *Climate Dyn.*, **18**, 255–276.
- Lengaigne, M., J.-P. Boulanger, C. Menkes, and H. Spencer, 2006: Influence of the seasonal cycle on the termination of El Niño events in a coupled general circulation model. *J. Climate*, in press.
- Lin, S.-J., 2004: A “vertically Lagrangian” finite-volume dynamical core for global models. *Mon. Wea. Rev.*, **132**, 2293–2307.
- Lock, A. P., A. R. Brown, M. R. Bush, G. M. Martin, and R. N. B. Smith, 2000: A new boundary layer mixing scheme. Part I: Scheme description and single-column model tests. *Mon. Wea. Rev.*, **128**, 3187–3199.
- Ma, C.-C., C. R. Mechoso, A. W. Robertson, and A. Arakawa, 1996: Peruvian stratus clouds and the tropical Pacific circulation: A coupled ocean–atmosphere GCM study. *J. Climate*, **9**, 1635–1645.
- McPhaden, M. J., and Coauthors, 1998: The Tropical Ocean–Global Atmosphere observing system: A decade of progress. *J. Geophys. Res.*, **103**, 14 169–14 240.
- Meehl, G. A., P. R. Gent, J. M. Arblaster, B. L. Otto-Bliesner, E. C. Brady, and A. Craig, 2001: Factors that affect the amplitude of El Niño in global coupled climate models. *Climate Dyn.*, **17**, 515–526.
- Moore, A. M., 1995: Tropical interannual variability in a global

- coupled GCM: Sensitivity to mean climate state. *J. Climate*, **8**, 807–828.
- Moorthi, S., and M. J. Suarez, 1992: Relaxed Arakawa–Schubert: A parameterization of moist convection for general circulation models. *Mon. Wea. Rev.*, **120**, 978–1002.
- Morel, A., and D. Antoine, 1994: Heating rate within the upper ocean in relation to its bio-optical state. *J. Phys. Oceanogr.*, **24**, 1652–1665.
- Neelin, J. D., 1991: The slow sea surface temperature mode and the fast-wave limit: Analytic theory for tropical interannual oscillations and experiments in a hybrid coupled model. *J. Atmos. Sci.*, **48**, 584–606.
- , D. S. Battisti, A. C. Hirst, F.-F. Jin, Y. Wakata, T. Yamagata, and S. Zebiak, 1998: ENSO theory. *J. Geophys. Res.*, **103**, 14 261–14 290.
- Norris, J. R., 1998: Low cloud type over the ocean from surface observations. Part II: Geographical and seasonal variations. *J. Climate*, **11**, 383–403.
- Philander, S. G. H., D. Gu, D. Halpern, G. Lambert, N.-C. Lau, T. Li, and R. C. Pacanowski, 1996: Why the ITCZ is mostly north of the equator. *J. Climate*, **9**, 2958–2972.
- Picaut, J., F. Masia, and Y. du Penhoat, 1997: An advective-reflective conceptual model for the oscillatory nature of the ENSO. *Science*, **277**, 663–666.
- Reynolds, R. W., N. A. Rayner, T. M. Smith, D. C. Stokes, and W. Wang, 2002: An improved in situ and satellite SST analysis for climate. *J. Climate*, **15**, 1609–1625.
- Rosow, W. B., and R. A. Schiffer, 1999: Advances in understanding clouds from ISCCP. *Bull. Amer. Meteor. Soc.*, **80**, 2261–2287.
- Simmons, A. J., and J. K. Gibson, 2000: The ERA-40 project plan. Tech. Rep., ERA-40 Project Report Series 1, ECMWF, Reading, United Kingdom, 63 pp.
- Smith, S. R., J. Servain, D. M. Legler, J. N. Stricherz, M. A. Bourassa, and J. J. O'Brien, 2004: Quantifying uncertainties in NCEP reanalyses using high-quality research vessel observations. *Bull. Amer. Meteor. Soc.*, **85**, 979–994.
- Smith, T. M., and R. W. Reynolds, 2003: Extended reconstruction of global sea surface temperatures based on COADS data (1854–1997). *J. Climate*, **16**, 1495–1510.
- Stockdale, T. N., A. J. Busalacchi, D. E. Harrison, and R. Seager, 1998: Ocean modeling for ENSO. *J. Geophys. Res.*, **103**, 14 325–14 355.
- Stouffer, R. J., and Coauthors, 2006: GFDL's CM2 global coupled climate models. Part IV: Idealized climate response. *J. Climate*, **19**, 723–740.
- Stricherz, J. N., D. M. Legler, and J. J. O'Brien, 1997: TOGA pseudostress atlas 1985–1994. II: Tropical Pacific Ocean. COAPS Tech. Rep. 97-2, COAPS/The Florida State University, Tallahassee, FL, 155 pp.
- Sun, D.-Z., and Coauthors, 2006: Radiative and dynamical feedbacks over the equatorial cold tongue: Results from seven atmospheric GCMs. *J. Climate*, in press.
- Sweeney, C., A. Gnanadesikan, S. M. Griffies, M. J. Harrison, A. J. Rosati, and B. L. Samuels, 2005: Impacts of shortwave penetration depth on large-scale ocean circulation and heat transport. *J. Phys. Oceanogr.*, **35**, 1103–1119.
- Trenberth, K. E., J. M. Caron, and D. P. Stepaniak, 2001: The atmospheric energy budget and implications for surface fluxes and ocean heat transports. *Climate Dyn.*, **17**, 259–276.
- Tudhope, A. W., and Coauthors, 2001: Variability in the El Niño–Southern Oscillation through a glacial-interglacial cycle. *Science*, **291**, 1511–1517.
- Vecchi, G. A., 2006: The termination of the 1997/98 El Niño. Part II: Mechanisms of atmospheric change. *J. Climate*, in press.
- , and D. E. Harrison, 2006: The termination of the 1997/98 El Niño. Part I: Mechanisms of oceanic change. *J. Climate*, in press.
- Wakata, Y., and E. S. Sarachik, 1994: Nonlinear effects in coupled atmosphere–ocean basin modes. *J. Atmos. Sci.*, **51**, 909–920.
- Wang, B., 1995: Interdecadal changes in El Niño onset in the last four decades. *J. Climate*, **8**, 267–285.
- , and X. Fu, 2001: Processes determining the rapid reestablishment of the equatorial Pacific cold tongue/ITCZ complex. *J. Climate*, **14**, 2250–2265.
- , and S.-I. An, 2002: A mechanism for decadal changes of ENSO behavior: Roles of background wind changes. *Climate Dyn.*, **18**, 475–486.
- , R. Wu, and X. Fu, 2000: Pacific–East Asian teleconnection: How does ENSO affect East Asian climate? *J. Climate*, **13**, 1517–1536.
- Wang, C., and R. H. Weisberg, 1996: Stability of equatorial modes in a simplified coupled ocean–atmosphere model. *J. Climate*, **9**, 3132–3148.
- Warren, S. G., C. J. Hahn, J. London, R. M. Chevin, and R. L. Jenne, 1988: Global distribution of total cloud cover and cloud type amounts over ocean. NCAR Tech. Note TN-317+STR, NCAR, Boulder, CO, 44 pp. [Available from the Carbon Dioxide Information Analysis Center, Oak Ridge, TN 37831.]
- Weng, F., N. C. Grody, R. Ferraro, A. Basist, and D. Forsyth, 1997: Cloud liquid water climatology from the Special Sensor Microwave/Imager. *J. Climate*, **10**, 1086–1098.
- Wittenberg, A. T., 2002: ENSO response to altered climates. Ph.D. thesis, Princeton University, 475 pp.
- , 2004: Extended wind stress analyses for ENSO. *J. Climate*, **17**, 2526–2540.
- Xie, P., and P. A. Arkin, 1996: Analyses of global monthly precipitation using gauge observations, satellite estimates, and numerical model predictions. *J. Climate*, **9**, 840–858.
- , and —, 1997: Global precipitation: A 17-year monthly analysis based on gauge observations, satellite estimates, and numerical model outputs. *Bull. Amer. Meteor. Soc.*, **78**, 2539–2558.
- Zebiak, S. E., and M. A. Cane, 1987: A model El Niño–Southern Oscillation. *Mon. Wea. Rev.*, **115**, 2262–2278.